

A Regression-Free Rainfall Estimation Algorithm for Dual-Polarization Radars

BIN PEI

Impact Forecasting, Aon Benfield, Chicago, Illinois

FIRAT Y. TESTIK

Civil and Environmental Engineering Department, The University of Texas at San Antonio, San Antonio, Texas

(Manuscript received 24 November 2017, in final form 5 June 2018)


ABSTRACT

In this study a new radar rainfall estimation algorithm—rainfall estimation using simulated raindrop size distributions (RESID)—was developed. This algorithm development was based upon the recent finding that measured and simulated raindrop size distributions (DSDs) with matching triplets of dual-polarization radar observables (i.e., horizontal reflectivity, differential reflectivity, and specific differential phase) produce similar rain rates. The RESID algorithm utilizes a large database of simulated gamma DSDs, theoretical rain rates calculated from the simulated DSDs, the corresponding dual-polarization radar observables, and a set of cost functions. The cost functions were developed using both the measured and simulated dual-polarization radar observables. For a given triplet of measured radar observables, RESID chooses a suitable cost function from the set and then identifies nine of the simulated DSDs from the database that minimize the value of the chosen cost function. The rain rate associated with the given radar observable triplet is estimated by averaging the calculated theoretical rain rates for the identified simulated DSDs. This algorithm is designed to reduce the effects of radar measurement noise on rain-rate retrievals and is not subject to the regression uncertainty introduced in the conventional development of the rain-rate estimators. The rainfall estimation capability of our new algorithm was demonstrated by comparing its performance with two benchmark algorithms through the use of rain gauge measurements from the Midlatitude Continental Convective Clouds Experiment (MC3E) and the Olympic Mountains Experiment (OLYMPEX). This comparison showed favorable performance of the new algorithm for the rainfall events observed during the field campaigns.

1. Introduction

The improvement of radar rainfall estimation has long been an active topic, as radar measurements play an important role in various applications related to meteorology, hydrology, and agriculture, among others (Sene 2009; Testik and Gebremichael 2010). Over the years a large number of dual-polarization radar algorithms for rain-rate estimations have been developed and tested (e.g., Seliga and Bringi 1976; Bringi and Chandrasekar 2001). These algorithms can be classified into two categories: (i) algorithms that estimate rain rates using functions (i.e., referred to as rain-rate estimators) that

depend on the dual-polarization radar observables [i.e. horizontal reflectivity (Z_h), differential reflectivity (Z_{dr}), and specific differential phase (K_{dp})] (category I); and (ii) algorithms that retrieve raindrop size distributions (DSDs) and use the retrieved DSDs to estimate rain rates via a rain-rate computation equation (category II; see details below). Typical examples of category I algorithms include Colorado State University–Hydrometeor Identification Rainfall Optimization (CSU-HIDRO) (Bringi and Chandrasekar 2001; Cifelli et al. 2011), the Joint Polarization Experiment (JPOLE) (Ryzhkov and Zrnić 1995, 1996; Ryzhkov et al. 2005a,b), Weather Surveillance Radar-1988 Doppler quantitative precipitation estimation (WSR-88D QPE) (Giangrande and Ryzhkov 2008; Vasiloff 2012; Berkowitz et al. 2013), the standard Next Generation Weather Radar (NEXRAD) (Fulton et al. 1998), and a number of others (e.g., Sachidananda and Zrnić 1987; Chandrasekar et al.

 Denotes content that is immediately available upon publication as open access.

Corresponding author: Dr. Firat Y. Testik, firat.testik@utsa.edu

DOI: 10.1175/JTECH-D-17-0201.1

© 2018 American Meteorological Society. For information regarding reuse of this content and general copyright information, consult the AMS Copyright Policy (www.ametsoc.org/PUBSReuseLicenses).

1993; Petersen et al. 1999; Cifelli et al. 2002; Bringi et al. 2009; Ryzhkov et al. 2014—based upon specific attenuation). Typical examples of category II algorithms are the algorithms developed by Zhang et al. (2001), Gorgucci et al. (2001, 2002), Bringi et al. (2002), Brandes et al. (2004a), Cao et al. (2010), Thurai et al. (2012), and Adirosi et al. (2014). In this study liquid precipitation (e.g., rain, drizzle) was our primary focus, and hence we implemented a hydrometeor classification to filter out other types of precipitation (see discussions in sections 2 and 3).

Although all of the algorithms mentioned above have been proven to perform at certain conditions, they were examined for errors introduced by parameterizations that were used in developing the rain-rate estimators and the DSD retrievals (e.g., Bringi and Chandrasekar 2001; Krajewski and Smith 2002; Thurai et al. 2012). In the development of a typical category I algorithm, the dual-polarization radar observables and the corresponding theoretical rain rates are first calculated using either the simulated or measured DSDs. The calculation of the dual-polarization radar observables relies on an accurate description of the electromagnetic scattering by particles. Computational techniques, such as the T-matrix method (Mishchenko et al. 1996), the discrete dipole approximation (Draine and Flatau 1994), and the Rayleigh formulas (see, e.g., Ryzhkov et al. 2011), have been widely used in determining the scattering amplitudes. Once the scattering amplitudes of raindrops are determined, the radar observables can be calculated. These calculations are based upon the assumption that raindrops follow a certain axis ratio–diameter relationship (e.g., Beard and Chuang 1987; Bringi et al. 2003; Beard et al. 2010). These calculations also incorporate assumptions about raindrop oscillations (typically implemented through canting angle distribution considerations; e.g., Beard and Jameson 1983; Bringi and Chandrasekar 2001) and temperature. Then, a large number of simulated dual-polarization radar observables and their theoretically calculated rain rates are utilized to derive the rain-rate estimators through nonlinear regression analyses (Bringi and Chandrasekar 2001; Ryzhkov et al. 2005a). As pointed out by a number of previous studies (e.g., Ciach et al. 2000; Krajewski and Smith 2002), the regression coefficients are highly sensitive to the ranges of the simulated radar observables, the sample size for the regression, and the data quality when measured DSDs are used. Moreover, for any given group of radar observables (e.g., Z_h and Z_{dr}), the derived rain-rate estimator can estimate the rain rate only as the value on the regression curve or surface, which would result in an uncertainty that is not typically accounted for.

Ideally, the aforementioned errors introduced by the data regression could be corrected by the use of category II algorithms with perfectly retrieved DSDs. This is because, in any category II algorithm, the rain rate is calculated using a theoretical equation that utilizes the DSD retrieved from the measured triplet of radar observables (i.e., Z_h , Z_{dr} and K_{dp}) (Zhang et al. 2001; Bringi et al. 2002). If the retrieval method for the DSD were flawless, the theoretical rain-rate equation, which is only a function of the DSD and raindrop fall velocity, would be able to provide a relatively accurate rain rate for a given triplet of radar observables. The rainfall estimation errors associated with the errors in raindrop fall velocities were discussed in great detail in Pei et al. (2014), but they are not a focus of this study. Nevertheless, the retrieval methods for DSDs have limitations and these limitations constrain the accuracy of the category II algorithms. Gorgucci et al. (2001, 2002) developed a method, which was later improved by Bringi et al. (2002), to retrieve gamma DSDs using the measured triplets of radar observables. In this method the normalized gamma DSD parameters (i.e., median volume diameter D_0 , normalized intercept parameter N_w , and shape parameter of a gamma distribution μ) were modeled as functions of radar observables. However, similar to the category I algorithms, these functions were derived using nonlinear regressions between simulated radar observables and the corresponding DSD parameters. Moreover, this method was reported to perform well only for radar observables within certain ranges of values and has a precision that is limited by the accuracy of the K_{dp} measurements (Brandes et al. 2004b). Note that measurement errors in K_{dp} values may reach up to 0.5°km^{-1} depending on the precipitation type, the number of radar samples, and the averaging range of the differential phase shift in K_{dp} calculations (Aydin et al. 1995; Ryzhkov and Zrnić 1996; Brandes et al. 2004b). Furthermore, K_{dp} measurements are not reliable when there is nonuniform beamfilling caused by a mixture of precipitation (WDTB 2011). To eliminate the effects of K_{dp} measurement errors in DSD retrievals, Zhang et al. (2001) proposed a method that uses a constrained gamma distribution to reduce the number of parameters (from three to two) that are required to represent a given DSD. In Zhang et al. (2001), the standard gamma DSD parameters (i.e., intercept parameter N_0 , slope parameter Λ , and μ) were retrieved from only Z_h and Z_{dr} measurements without using K_{dp} measurements. Although the effects of K_{dp} measurement errors in DSD retrievals were eliminated, the constrained gamma distribution in Zhang et al.'s algorithm was also developed through a regression analysis and may be challenged by the DSDs that have significant

concentration differences between larger and smaller raindrops (Brandes et al. 2004a,b). For example, the constrained gamma distribution may not be applied to the DSDs with large populations of larger drops and small populations of smaller drops, such as those that may be observed in the leading edges of some convective storms (Brandes et al. 2004a).

In this study we developed a new algorithm that takes advantage of the benefits of both category I and category II algorithms to provide more accurate rainfall estimates. Recently, Adirosi et al. (2014) introduced a method to evaluate the accuracy of the gamma DSD assumption in radar rainfall estimations. In their study the rain rates that were estimated using the measured DSDs and the simulated ones that follow gamma distributions were compared. The simulated gamma DSD that corresponds to the measured one was considered to be the simulated DSD with the smallest cost function value. The cost function was defined using the triplet of dual-polarization radar observables. Adirosi et al. concluded that errors associated with the gamma DSD assumption exist, but they showed that these errors were reasonably small, especially at the S band (see Fig. 4 of Adirosi et al. 2014), which is the focus of this study. Similar to Adirosi et al. (2014), cost functions have been utilized in other studies for DSD retrievals and rain-rate estimations. In one such study, Cao et al. (2010) performed dual-polarization radar rainfall estimation through the retrieval of DSD using the Bayesian approach. In their study rain rate was estimated from a gamma DSD, which was constructed using mean and standard deviations of the conditional distributions of the DSD parameters retrieved through the Bayesian approach. In another study, Posselt et al. (2015) analyzed the information content of the selected dual-polarization radar observables in the mixed- and ice-phase regions of a convective storm. Both observational and modeling uncertainties of the radar observables were quantified using the Bayesian approach similar to that implemented in Cao et al. (2010). The likelihood equation, which may be considered equivalent to a cost function, was utilized in both studies. Here, we developed a new rain-rate estimation algorithm by using a large database of simulated gamma DSDs and a series of selected cost functions without a regression analysis. We concluded that for any given triplet of measured dual-polarization radar observables, simulated DSDs with similar rain rates as the “real” DSD can be identified using an appropriate cost function. Therefore, these simulated DSDs can be used to estimate the rain rate. To demonstrate the improved accuracy of rain-rate retrievals using this proposed algorithm, a comparative analysis was conducted using rain gauge measurements and two benchmark radar rainfall estimation algorithms.

This paper is organized as follows: the proposed algorithm along with the two benchmark algorithms are introduced in section 2, the radar and rain gauge measurement data utilized in this study are discussed in section 3, the results and discussions are presented in section 4, and the summary and conclusions are provided in section 5.

2. Methodology

A new radar rainfall estimation algorithm—rainfall estimation using simulated DSDs (RESID)—was developed and compared with two benchmark algorithms: CSU-HIDRO (Bringi and Chandrasekar 2001; Cifelli et al. 2011) and WSR-88D QPE (Giangrande and Ryzhkov 2008; Vasiloff 2012; Berkowitz et al. 2013). Details of these three algorithms are discussed in this section. Without further notice, all formulations given in this article are for the S-band radar with 10-cm wavelength. Note that, other than S-band radar, conventional scanning weather radars with different wavelengths (e.g., C and X bands) are also used in rainfall estimations. The weather radars that operate on a shorter wavelength (e.g., X band) than the S-band radars are more sensitive to the surroundings and attenuation in shorter distances. Moreover, for such radars, increased sensitivity to the differential phase shift has more pronounced effects on measurements during rainfall events that are composed of small spherical raindrops (e.g., low rain-rate events). Therefore, although such radars can detect smaller particles (e.g., cloud drops), they are suitable for observations within a shorter range and for certain environmental conditions.

a. CSU-HIDRO

The CSU-HIDRO rainfall retrieval algorithm utilizes a combination of four rain-rate estimators as presented in Fig. 1 (reproduced from Cifelli et al. 2011). These estimators are $R(Z_h)$, $R(K_{dp})$, $R(Z_h, Z_{dr})$, and $R(K_{dp}, Z_{dr})$. The empirical formulations for these estimators are given as follows (Bringi and Chandrasekar 2001):

$$R(Z_h) = 0.017(Z_h)^{0.7143}, \quad (1)$$

$$R(K_{dp}) = 50.7(K_{dp})^{0.85}, \quad (2)$$

$$R(Z_h, Z_{dr}) = 6.7 \times 10^{-3} (Z_h)^{0.927} 10^{(-0.343Z_{dr})}, \quad (3)$$

$$R(K_{dp}, Z_{dr}) = 90.8(K_{dp})^{0.93} 10^{(-0.169Z_{dr})}. \quad (4)$$

Here, R is the rain rate (mm h^{-1}), which is modeled as functions of the abovementioned dual-polarization radar observables Z_h ($\text{mm}^6 \text{m}^{-3}$), Z_{dr} (dB) and K_{dp} ($^\circ \text{km}^{-1}$). These empirical formulations were derived through

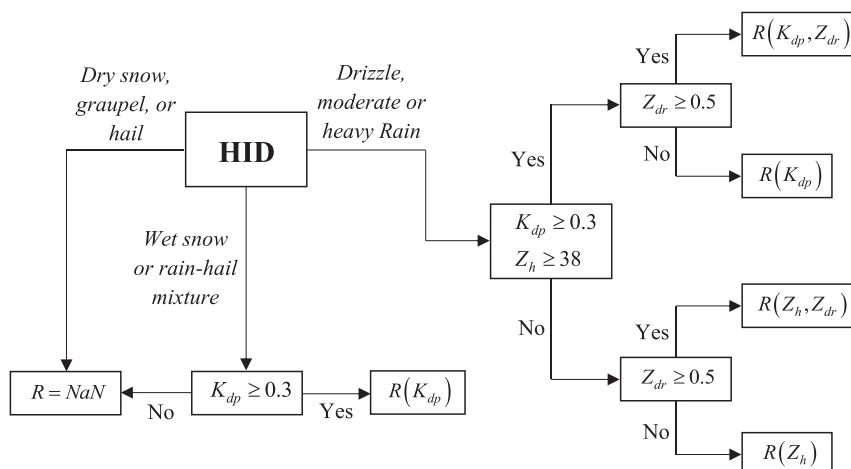


FIG. 1. CSU-HIDRO rainfall retrieval algorithm, with radar observables Z_h (dBZ), Z_{dr} (dB), and K_{dp} ($^{\circ}\text{km}^{-1}$).

nonlinear regressions as described in the previous section. Details of the derivation procedure can be found in [Bringi and Chandrasekar \(2001\)](#) and [Pei et al. \(2014\)](#). Using the CSU-HIDRO algorithm, the rain rate can be estimated for any given triplet of radar observables (see [Fig. 1](#)). Since the focus of this study was liquid rainfall, a hydrometeor identification (HID) algorithm was required to be able to filter out solid precipitation that may occur during severe convective storms and cold-season precipitation events. We used the WSR-88D hydrometeor classification algorithm (HCA; see the discussion in the next subsection) to identify different precipitation types for the CSU-HIDRO, the WSR-88D QPE, and the RESID algorithms. It should be noted that CSU-HIDRO has its own HID algorithm (see [Fig. 1](#)) that utilizes a fuzzy logic technique to classify precipitation types ([Lim et al. 2005](#); [Cifelli et al. 2011](#); [Dolan et al. 2013](#)). However, for a fair comparison, the HCA was implemented consistently among all of the rain-rate estimation algorithms.

b. WSR-88D QPE

The WSR-88D QPE algorithm uses only one rain-rate estimator for liquid rainfall estimations. This estimator is $R(Z_h, Z_{dr})$ [Eq. (3)], which was adopted from the CSU-HIDRO rainfall retrieval algorithm ([Vasiloff 2012](#); [Berkowitz et al. 2013](#)). This estimator [Eq. (3)] replaced the initial estimator that was developed as part of JPOLE ([Giangrande and Ryzhkov 2008](#)) because it produces rainfall estimates that are more accurate for Southeast storms than the initial estimator ([Vasiloff 2012](#)). Along with the HCA, the WSR-88D QPE algorithm uses Eq. (1) and the following estimator given in Eq. (5) to estimate the mixed and cold-season precipitation (e.g., hail, snow, graupel):

$$R(K_{dp}) = 44|K_{dp}|^{0.822} \text{sign}(K_{dp}), \quad (5)$$

where $\text{sign}(K_{dp})$ is the signum function that indicates the sign (positive or negative) of the K_{dp} value. The details of the WSR-88D QPE algorithm can be found in [Giangrande and Ryzhkov \(2008\)](#) and [Berkowitz et al. \(2013\)](#). In these publications the HCA was reported to be capable of identifying 10 different types of meteorological and nonmeteorological classifications, including light and moderate rain, a mixture of rain and hail, wet snow, graupel, ice crystal, and ground clutter. In this study we did not conduct the calculations [i.e. using the equations; e.g., Eq. (3), and the HCA] to estimate the rain rates for the WSR-88D QPE algorithm. Instead, we used the precipitation products available from the National Climatic Data Center (NCDC; see [section 3](#) for details). These products were produced using the HCA and the abovementioned equations, and were widely utilized by the weather and radar communities. It should be noted that these products using the WSR-88D QPE algorithm consider radar observables measured at different elevation angles to optimize the rainfall estimations for different clutter, exclusion zone, and beam blockage conditions ([WDTB 2011](#)). However, optimization of the rainfall estimations at different elevation angles is beyond the scope of this study and was not implemented here for the CSU-HIDRO and RESID estimations. Therefore, for CSU-HIDRO and RESID, we used the radar observables measured at the lowest elevation angle (0.5°) to estimate the radar rainfall.

c. RESID

The RESID algorithm was developed to improve the rain-rate estimations using the current dual-polarization

weather radars. The fundamental basis of this algorithm is that, for any given measured triplet of dual-polarization radar observables, a simulated DSD (with a calculated triplet of radar observables that is similar to the measured one) can be utilized to estimate the rain rate. The rain-rate estimation error using this approach has been shown to be fairly small if the triplet calculated from the simulated DSD is sufficiently close to the measured one (Adirosi et al. 2014). We implemented the following three-step approach to develop the RESID algorithm for improved radar rain-rate estimations. It should be noted that, because of the radar observational uncertainties (e.g., measurement error in K_{dp}), the actual observed DSD and the simulated DSD with the matching triplets may differ (see Adirosi et al. 2014 and McFarquhar et al. 2015). Our study (and the RESID) did not address these radar observational uncertainties explicitly; however, we expect that their impacts on rain-rate estimates are reduced, as the RESID utilizes an optimization scheme in cost function selection. Moreover, the RESID addressed the uncertainties from the parameterization/regression analyses in developing the category I and II algorithms.

1) STEP 1: DSD SIMULATIONS

A large number of simulated DSDs, their calculated triplets of radar observables, and the corresponding theoretical rain rates are required for the implementation of the RESID algorithm. The purpose of the DSD simulations is not to develop a database of realistic DSDs but to cover a wide range of DSD possibilities (Adirosi et al. 2014). In radar rainfall estimations, DSDs are typically modeled as gamma distributions (Ulbrich 1983). In this study the gamma distribution assumption was adopted and the normalized gamma DSDs were utilized. Proposed by Willis (1984), the normalized gamma DSD can be expressed as follows:

$$N(D) = N_w \frac{6}{3.67^4} \frac{(3.67 + \mu)^{\mu+4}}{\Gamma(\mu+4)} \left(\frac{D}{D_0}\right)^\mu \times \exp\left[-(3.67 + \mu)\frac{D}{D_0}\right], \quad (6)$$

where $N(D)$ is the DSD, which represents the number of drops in a unit volume (m^3) and a unit interval of the equivalent-volume drop diameter D (mm); $\Gamma()$ is the complete gamma function; and N_w ($\text{mm}^{-1}\text{m}^{-3}$), D_0 (mm), and μ (unitless) are the aforementioned normalized gamma DSD parameters. Using Eq. (6), a database of simulated gamma DSDs can be formed by varying the values of the normalized gamma DSD parameters (i.e., N_w , D_0 , and μ). In this study $\log_{10}(N_w)$, D_0 , and μ were uniformly varied with a 0.03 increment over the ranges

from 1 to 7 (for N_w ; $\text{mm}^{-1}\text{m}^{-3}$), from 0.5 to 3.5 mm, and from -3.4 to 20 , respectively (e.g., D_0 values were varied as 0.5, 0.53, 0.56, ..., 3.5 mm). Note that these proposed ranges were mostly adopted from Adirosi et al. (2014), who performed a relevant sensitivity analysis. However, we set the lower bound of μ as -3.4 instead of -4 , because when the μ value is between -3.67 and -4 , Eq. (6) generates complex numbers. Moreover, unlike Adirosi et al. (2014), a fixed increment, rather than random sampling, was used to guarantee the entire DSD simulation domain was densely covered. By doing so, more than 10 million DSDs were simulated as opposed to Adirosi et al. (2014), who used over 80 000 DSDs.

Once the database of simulated DSDs was constructed, the corresponding dual-polarization radar observables and theoretical rain rates were calculated. The dual-polarization radar observables were computed using the T-matrix method (Leinonen 2014). In our computations, the minimum and maximum drop diameters were set as 0 and 8 mm, respectively. The dielectric constant of water was taken at 20°C from Ray (1972) as suggested by Bringi and Chandrasekar (2001). Temperature variation was not considered in the calculations. It was assumed that raindrops follow the equilibrium shape proposed by Beard and Chuang (1987) and that the raindrop canting angles follow a normal distribution with a 0° mean and a 7° standard deviation (Bringi and Chandrasekar 2001). The equilibrium shape model by Beard and Chuang (1987) was described using the following polynomial fit:

$$\alpha = \frac{b}{a} = 1.0048 + 5.7 \times 10^{-4}D - 2.628 \times 10^{-2}D^2 + 3.682 \times 10^{-3}D^3 - 1.677 \times 10^{-4}D^4, \quad (7)$$

where α is the axis ratio, defined as the ratio of the semi-minor (b) to the semimajor (a) axis lengths of the equilibrium raindrop shape; and D is in millimeters. It should be noted that raindrops observed in both artificial and natural rainfall experiments indicated that raindrop axis ratios may deviate from the equilibrium predictions by Beard and Chuang (e.g., Gorgucci et al. 2000; Thurai et al. 2007). Equation (7) was still used, however, because it is a widely accepted formulation in the radar community. In our calculations the theoretical rain rates that correspond to the simulated DSDs were determined using

$$R = 0.6\pi \times 10^{-3} \int_0^\infty v D^3 N(D) dD, \quad (8)$$

where v is the raindrop fall velocity (m s^{-1}). A commonly used approach is to assume that raindrops fall at terminal velocity v_t . Here, we represented raindrop fall velocities using the following terminal

velocity parameterization (m s^{-1}) proposed by Atlas and Ulbrich (1977):

$$v_t = 3.78D^{0.67}, \quad (9)$$

where D is in millimeters. Note that this power-law equation [Eq. (9)] was utilized mainly because of its simplicity. A more complex terminal velocity parameterization, such as the exponential relation developed by Atlas et al. (1973), may be preferred for potential accuracy improvements. It can be considered that the use of this simpler and potentially less accurate power-law equation in RESID estimations in this study resulted in a potentially more conservative comparison of the RESID's capabilities with those of the two benchmark algorithms. Substituting Eqs. (6) and (9) into Eq. (8) yields

$$R = (0.6\pi \times 10^{-3})(3.78)N_w f(\mu) \Gamma(4.67 + \mu) \times \frac{D_0^{4.67}}{(3.67 + \mu)^{4.67 + \mu}}, \quad (10)$$

where

$$f(\mu) = \frac{6}{3.67^4} \frac{(3.67 + \mu)^{\mu+4}}{\Gamma(\mu + 4)}. \quad (11)$$

To eliminate the simulations with unrealistically large rain rates, DSDs that result in theoretical rain rates larger than 300 mm h^{-1} were removed from the database (Bringi and Chandrasekar 2001; Gorgucci et al. 2008).

2) STEP 2: COST FUNCTION SELECTION

The cost functions are a critical component of the RESID algorithm. For a given measured triplet of radar observables, the representative DSDs can be identified from the database developed in step 1 by minimizing the selected cost function value. The cost functions are modeled using the measured and simulated radar observables. Adirosi et al. (2014) utilized a single cost function for their application as defined below:

$$\text{CF} = \frac{(Z_{h,m} - Z_{h,s})^2}{\bar{Z}_{h,s}} + \frac{(Z_{dr,m} - Z_{dr,s})^2}{\bar{Z}_{dr,s}} + \frac{(K_{dp,m} - K_{dp,s})^2}{\bar{K}_{dp,s}}, \quad (12)$$

where CF is the cost function; subscripts m and s stand for the measured and simulated radar observables, respectively; and $\bar{Z}_{h,s}$, $\bar{Z}_{dr,s}$, and $\bar{K}_{dp,s}$ are the mean values of the simulated radar observables. In radar measurements, however, when the Z_h value is small (e.g., $< 38 \text{ dBZ}$), Z_{dr} and K_{dp} are generally noisy. The measurement noise also becomes an issue when the K_{dp} value is small (e.g., $< 0.3^\circ \text{ km}^{-1}$) or when its standard deviation falls

between 0.3° and $0.4^\circ \text{ km}^{-1}$ given how K_{dp} is derived (Bringi and Chandrasekar 2001). Therefore, using the single cost function provided in Eq. (12) alone may lead to inaccurate rainfall estimates. Adirosi et al. (2014) addressed this issue by utilizing an interpolation function along with Eq. (12) in order to reduce the DSD selection error near the edges of the simulation domain where the simulated triplets are thinly dispersed. In this study we proposed a solution by incorporating a group of modified cost functions that use a varying number (i.e., 1, 2, or 3) of the radar observables (i.e., Z_h , Z_{dr} , and K_{dp}). The purpose was to reduce the effect of the radar measurement noise by selecting a suitable cost function for the given values of the measured radar observables. The general form of the RESID cost functions is given below:

$$\text{CF}(X_1, X_2, \dots, X_n) = \sum_{i=1}^n \frac{(X_{i,m} - X_{i,s})^2}{\bar{X}_{i,s}}, \quad (13)$$

where X_1, X_2, \dots, X_n are the dual-polarization radar observables (i.e., Z_h , Z_{dr} , and K_{dp}) with the n value varying from 1 to 3; $X_{i,m}$ is the measured radar observable; and $\bar{X}_{i,s}$ is the mean value of the simulated radar observable $X_{i,s}$. The cost functions are named as single-, double-, and triple-measurement cost functions as determined by the value of n . For example, the cost function $\text{CF}(Z_h, Z_{dr})$, which is expressed as $[(Z_{h,m} - Z_{h,s})^2 / \bar{Z}_{h,s}] + [(Z_{dr,m} - Z_{dr,s})^2 / \bar{Z}_{dr,s}]$, is a double-measurement cost function. It should be noted that these new cost functions do not address the radar observational uncertainty as discussed earlier, which may also result from radar calibration errors, etc.

3) STEP 3: ALGORITHM IMPLEMENTATION

We adopted the radar observable thresholds (see Fig. 1) utilized in the CSU-HIDRO rainfall retrieval algorithm to implement the RESID cost functions. These thresholds were derived to differentiate radar signals from noise and to maximize the performance of the rain-rate estimators (Bringi et al. 1996; Petersen et al. 1999; Cifelli et al. 2011). The complete RESID algorithm is illustrated in Fig. 2. As can be seen in this figure, for any given triplet of measured radar observables (i.e., $Z_{h,m}$, $Z_{dr,m}$ and $K_{dp,m}$), a cost function is first selected. This cost function is then used along with the simulated radar observables (i.e., $Z_{h,s}$, $Z_{dr,s}$, and $K_{dp,s}$) to locate the simulated DSDs that have the smallest cost function values. During the development of the RESID using a sample dataset, we found out that when the minimum value of the triple-measurement cost function [i.e. $\text{CF}(Z_h, Z_{dr}, K_{dp})$] was larger than 0.1 ($\sim 1\%$ of the sample dataset), the double-measurement cost function [i.e. $\text{CF}(Z_{dr}, K_{dp})$] provided more accurate results.

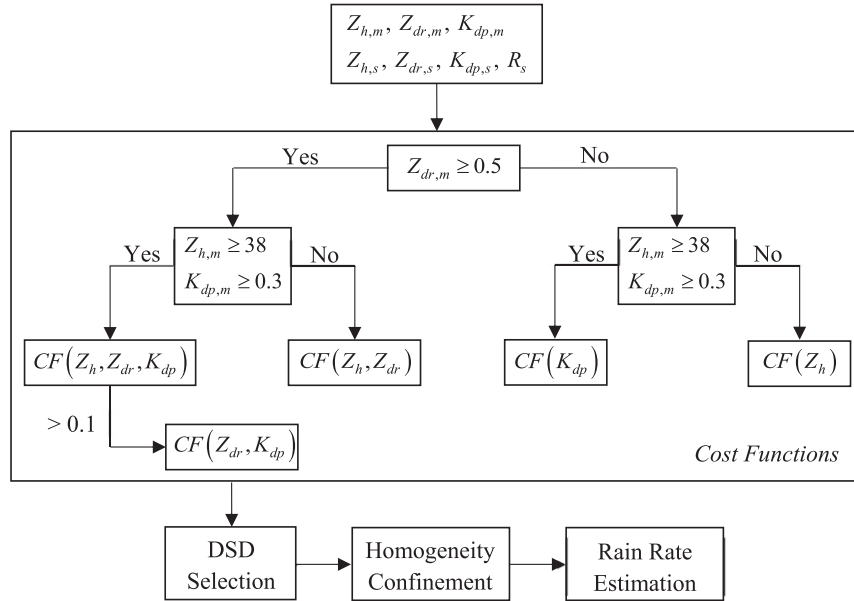


FIG. 2. Flowchart of RESID rain-rate estimation algorithm, with radar observables Z_h (dBZ), Z_{dr} (dB), and K_{dp} ($^{\circ}\text{km}^{-1}$).

Therefore, in the implementation of the algorithm, when the minimum value of the triple-measurement cost function is larger than 0.1, the double-measurement cost function is utilized (see Fig. 2). Once the cost function value is computed for each of the simulated DSDs, nine of them that have the smallest cost function values are selected. Then, the homogeneity around these DSDs is checked. Adirosi et al. (2014) suggested that the DSDs are not homogeneous when the difference between their maximum and minimum theoretically calculated rain rates (R_s) is larger than 15 mm h^{-1} . In this study we did not adopt their homogeneity criterion because a fixed spread value of the calculated rain rate may not be suitable for rainfall events with different intensities. We observed that, in most inhomogeneous cases, the selected DSDs have both positive and negative gamma shape parameters (μ). This is because the DSD with either a positive or a negative μ value can have similar calculated radar observable triplets. However, the rain rate associated with the DSD that has a negative μ value is usually much higher than the DSD that has a positive μ value. Therefore, in the implementation of the RESID algorithm, to confine homogeneity among the selected DSDs, the DSDs with a smaller count of the shape parameters that have the same sign (i.e., either positive or negative) are discarded. For example, out of the nine selected simulated DSDs with the smallest cost function values, if three of them have negative μ values, these three DSDs are discarded and the remaining six DSDs with positive μ values are kept. This criterion resulted in

less than 1% of the selected DSDs not being homogeneous in our analysis. Such a homogeneity confinement criterion ensured more accurate estimations of the rain rates for the cases with selected DSDs that correspond to significantly different rain rates. Finally, the rain rate for the measured triplet of radar observables is estimated by taking the average of the calculated rain rates from the remaining selected DSDs. Note that there is a set methodology in implementing the RESID algorithm as described in this section. In the implementation of this methodology for the datasets considered in this study (sections 3 and 4), this methodology was not altered by the ground truth (i.e., rain gauge measurement) or other such parameters that would favor a biasing effect on the results.

3. Data description

To evaluate the performance of the RESID, the CSU-HIDRO, and the WSR-88D QPE algorithms, large datasets from two major field campaigns were utilized. The first dataset includes the dual-polarization WSR-88D observations from the Vance Air Force Base, Oklahoma (KVNXX), and the rain gauge measurements during the Midlatitude Continental Convective Clouds Experiment (MC3E) (Jensen et al. 2016). The second dataset includes the radar measurements from the dual-polarization WSR-88D at Langley Hill, Washington (KLGX), and the rain gauge observations during the Olympic Mountains Experiment (OLYMPEX) (Houze et al. 2017). The

two field campaigns were selected to consider different meteorological conditions in our comparative study. Mostly convective and orographic precipitation was observed during MC3E and OLYMPEx, respectively. Tropical precipitation was not part of these field campaigns. The rain gauges deployed in these field campaigns were model 370/380 gauges manufactured by Met One Instruments, Inc. (Global Hydrology Resource Center 2017). The accuracy of this rain gauge model is $\pm 0.5\%$ at 0.5 in. h^{-1} (12.7 mm h^{-1}) rainfall and $\pm 1\%$ at $1.0\text{--}3.0 \text{ in. h}^{-1}$ ($25.4\text{--}76.2 \text{ mm h}^{-1}$) rainfall (Met One Instruments Inc. 2017).

The MC3E was held in central Oklahoma between April and June 2011. It was a joint campaign between the National Aeronautics and Space Administration (NASA) and the Department of Energy Atmospheric Radiation Measurement Climate Research Facility. It was partly to serve NASA's Ground Validation program for the Global Precipitation Measurement (GPM) mission. Instruments deployed in MC3E included aircraft- and ground-based instruments that aimed at providing a comprehensive visualization of the three-dimensional meteorological environment (Jensen et al. 2016). Our analyses utilized the data from the KVNIX WSR-88D (S-band radar with a frequency of $\sim 3 \text{ GHz}$) and the 16 rain gauge pairs. The locations of these instruments are shown in Fig. 3a. The distances from the radar to the rain gauge pairs were from 53 to 65 km. The radar data were obtained from NCDC. We used the quality-controlled level-III products, which included Z_h , Z_{dr} , K_{dp} , the correlation coefficient (ρ_{HV}), the hydrometeor classification (HC), and the digital precipitation rate (DPR). These products were available as digital images. A special decoder was used to convert them into a commonly used scientific data format. Except for the DPR, all other products were measured at 0.5° elevation angle. The ρ_{HV} is the correlation coefficient between the radar's horizontal and vertical polarizations, and it was utilized to distinguish non-meteorological echoes. The HCs were used to identify different particle types. The rainfall accumulations calculated using the DPRs (based upon the WSR-88D QPE algorithm) were utilized for comparisons with the rainfall accumulations that were estimated using other algorithms (i.e., CSU-HIDRO and RESID). In this study all of the radar measurements in any range bin with a ρ_{HV} value less than 0.85 (i.e., nonmeteorological echo) were discarded (Ryzhkov et al. 2005a). The radar measurements classified as any particle type other than precipitation (e.g., ground clutter, biological scatterers) were not considered either. During MC3E, rainfall accumulations were measured using 32 rain gauges that were paired at 16 locations to reduce measurement artifacts (see Fig. 3a). The quality-controlled rainfall

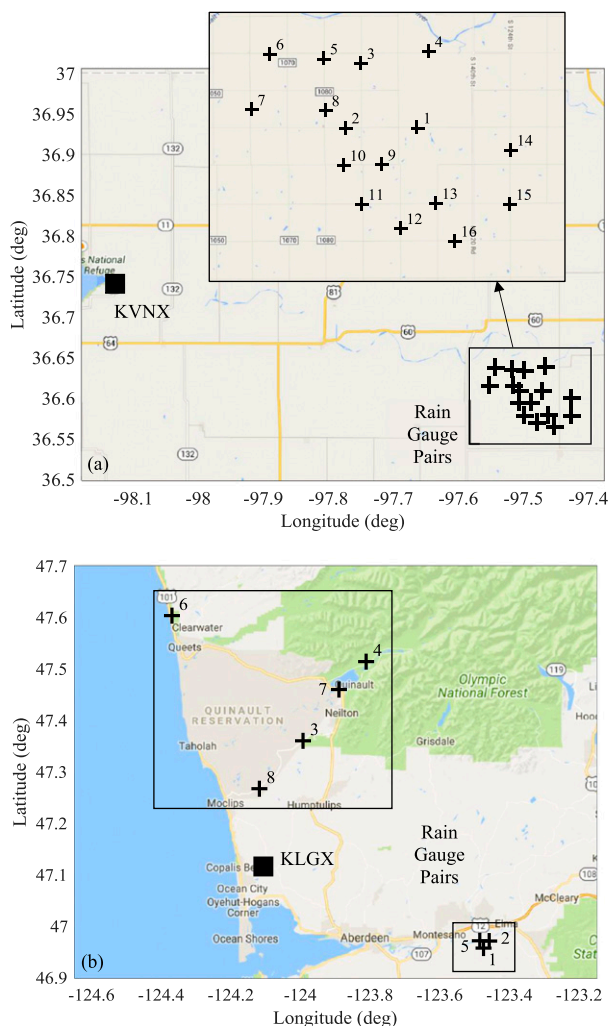


FIG. 3. Locations of (a) KVNIX radar and 16 rain gauge pairs in MC3E and (b) KLGX radar and 8 rain gauge pairs in OLYMPEx (background images from Google Map).

amount data from the 16 rain gauge pairs was averaged for each pair at 1-min intervals and summed up to form hourly accumulations that were used in the subsequent analyses. For the time periods when there was only one rain gauge measurement available, no averaging was performed; and when both rain gauge measurements were missing, the corresponding radar observations were not considered. The rain gauge data in MC3E were mainly from five days of measurements, namely, 24, 25, and 27 April, and 11 and 20 May 2011 (UTC). Note that an intense convective event that occurred in the late morning of 20 May (see Petersen and Jensen 2012) was excluded in our analysis because of inadequate radar observations. This event was associated with high rainfall intensities with rapidly changing rain rates between sequential radar scans. For this event a comparison between the

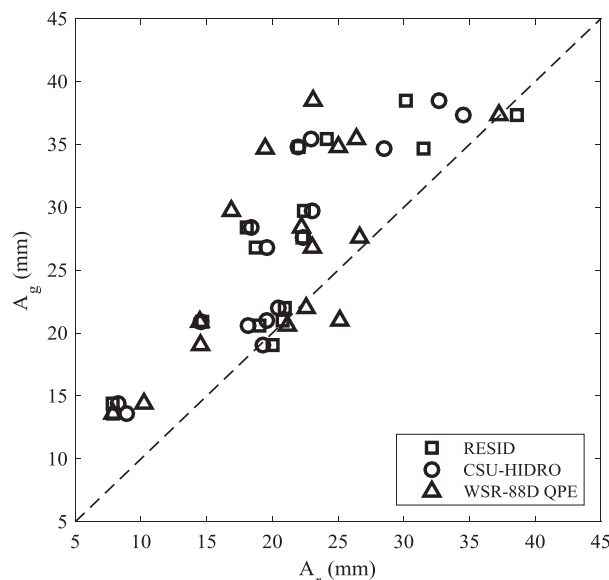


FIG. 4. Comparison between A_g and A_r for the convective rainfall event of 20 May 2011. Symbols in this figure represent 1-h rainfall accumulation values from different rain gauges (total of 16 rain gauges in MC3E) and the corresponding radar retrievals using RESID, CSU-HIDRO, and WSR-88D QPE algorithms (see the legend).

rain gauge-measured (A_g) and the radar-estimated (A_r) hourly rainfall accumulations is presented in Fig. 4. As can be seen in Fig. 4, the rainfall estimation errors for this specific rainfall event are significant regardless of the algorithm.

The second dataset utilized in this study was from the KLGX radar (S-band radar with a frequency of ~ 3 GHz) and the rain gauge pairs deployed in the OLYMPEx field campaign. OLYMPEx was held on the Olympic Peninsula of Washington State between November 2015 and February 2016, and it is one of the latest field campaigns led by NASA for the GPM Ground Validation program. This field campaign focused on rainfall enhancement through orographic lifting and assessment of precipitation measurements from the GPM satellite (Houze et al. 2017). Radar rainfall estimations may be influenced by the beam blockage caused by orography. Each WSR-88D uses a local terrain file and a hybrid scan technique (Berkowitz et al. 2013) to determine the percentage of beam blockage (WDTB 2011). While an optimization scheme is implemented in WSR-88D QPE to reduce the influence of beam blockage, such a scheme is not implemented in RESID and CSU-HIDRO (see the discussion in section 2). Therefore, screening for radar beam blockage was essential in the evaluation of the algorithms. For the screening we used the beam blockage map provided by Mass (2011). The rain gauges in OLYMPEx with more than 50% beam blockage at 0.5° elevation angle were

not considered in our analyses. The beam blockage percentage value of 50% is the threshold value used by the WSR-88D QPE algorithm to optimize the liquid rainfall estimation (WDTB 2011). Removing rain gauges at locations with beam blockage percentages that are larger than 50% ensured that, consistent with the estimations by the other two algorithms, the WSR-88D QPE estimations used data from the 0.5° elevation angle. This screening process resulted in 16 rain gauges paired at eight locations for the subsequent analyses. The locations of the KLGX radar and the eight rain gauge pairs are shown in Fig. 3b. The distances from the KLGX radar to the rain gauge pairs were between 17 and 58 km. The KLGX radar data utilized in this study were similar to the KVNIX radar data used, and the same methods were employed to distinguish non-meteorological echoes and to remove nonprecipitation measurements as discussed above. Similarly, the same data analysis methodology was implemented on the rain gauge measurements to assemble the hourly rainfall accumulations. Five days of moderate rainfall events [i.e., 13 and 17 November, and 8 December 2015; and 21 and 28 January 2016 (UTC)] with the highest daily rain totals during OLYMPEx were selected for our comparative analyses, detailed in the next section. The daily rain totals were calculated as the summation of the daily rainfall accumulations for the abovementioned eight rain gauge pairs.

4. Results and discussion

The hourly rainfall accumulations estimated using the RESID, the CSU-HIDRO, and the WSR-88D QPE algorithms were compared with the rain gauge measurements at 16 locations in MC3E and 8 locations in OLYMPEx. To smooth the radar measurements at every rain gauge location, rain rates from 10 radar gates that were closest to the rain gauge were first estimated. These radar gates were at two adjacent azimuth angles around the given rain gauge (i.e., five radar gates closest to the rain gauge for each of the azimuth angle). For the WSR-88D QPE estimations, these rain rates were obtained from the WSR-88D level-III precipitation products as discussed in section 3. For the RESID and the CSU-HIDRO estimations, the rain rates were estimated using the methodology described in section 2 for the dual-polarization radar observables measured at the 0.5° elevation angle. Note that the radar measurements that correspond to any precipitation type other than liquid precipitation (e.g., mixed precipitation) were removed from the analyses. Only 0.3% and 1.5% of the radar scans that detected precipitation for MC3E and OLYMPEx, respectively, were identified as mixed or cold-season

precipitation. Then, the mean value of the estimated rain rates from the five closest radar gates at two adjacent azimuth angles (10 gates in total) was computed, and this mean value was treated as the rain rate for that particular rain gauge location. By doing this, the rain rates were averaged roughly over an area of $1 \text{ km} \times 1^\circ$ (Ryzhkov et al. 2005a). To estimate the rain rates in between the two subsequent radar observations, linear interpolation was performed. In the case of no missing radar scans, the time interval between two subsequent scans varies with the severity of the event. For clear-air, snow, and light stratiform events, the interval is usually 10 min. For severe convective events, the interval can reduce to as low as 4.5 min (NWS 2017a). If there is a missing scan, linear interpolation between the two subsequent radar scans was still performed to estimate the rain rates. These rain rates were then used to calculate the rainfall accumulations corresponding to the hourly rain gauge measurements.

The performance of the three algorithms in radar rainfall estimation was examined by comparing the radar-estimated rainfall accumulations with the rain gauge measurements and these comparisons were quantified statistically. The statistical quantities that were utilized in this study included the normalized bias (NB), the normalized standard error (NSE), and the Pearson correlation coefficient (CORR). The respective mathematical formulations are given below:

$$\text{NB} = \frac{\overline{A_r} - \overline{A_g}}{\overline{A_g}} \times 100\%, \quad (14)$$

$$\text{NSE} = \frac{\sqrt{(A_r - A_g)^2}}{\overline{A_g}} \times 100\%, \quad (15)$$

$$\text{CORR} = \frac{\text{cov}(A_r, A_g)}{\sigma_{A_r} \sigma_{A_g}}, \quad (16)$$

where A_r and A_g are the radar-estimated and the gauge-measured hourly rainfall accumulations, respectively; $\overline{A_r}$ and $\overline{A_g}$ are the mean values of A_r and A_g , respectively; $(A_r - A_g)^2$ is the averaged square error between A_r and A_g ; $\text{cov}(A_r, A_g)$ is the covariance between A_r and A_g ; and σ_{A_r} and σ_{A_g} are the standard deviations of A_r and A_g , respectively.

The results of our comparisons at three sample locations each for MC3E and OLYMPEx are presented in Figs. 5 and 6, respectively. The three locations used in these figures were purposefully selected far away from each other (see Fig. 3). The statistics for rainfall accumulations at all locations of MC3E and OLYMPEx are provided in Tables 1 and 2, respectively. The statistics

from gauge 9 in MC3E were not included in the calculations of the mean statistics because of inadequate data samples (see Table 1). As can be clearly seen from Figs. 5 and 6 as well as from Tables 1 and 2, the RESID algorithm outperforms the CSU-HIDRO and the WSR-88D QPE algorithms in terms of estimating the hourly rainfall accumulations. Detailed findings are summarized below.

- 1) As presented in Fig. 5, the rainfall estimation results obtained by using RESID agree well with the rain gauge measurements; however, CSU-HIDRO and WSR-88D QPE tend to overestimate the rainfall accumulations. Moreover, RESID estimates the rainfall accumulations with a smaller scatter (random error) than those that were estimated using CSU-HIDRO and WSR-88D QPE. As given in Table 1 for MC3E, both the NB and NSE values for RESID estimations are significantly lower than the NB and the NSE values for CSU-HIDRO and WSR-88D QPE estimations. For example, the rainfall accumulations estimated using RESID have a mean NB value of -2.5% , whereas the mean NB values for CSU-HIDRO and WSR-88D QPE are 34.4% and 25.8% , respectively. Nevertheless, all three algorithms performed well in terms of their CORR values. Almost all CORR values (see Tables 1 and 2) are larger than 0.8, which indicates a strong positive correlation between the estimated and the measured rainfall accumulations. Although rain gauges were relatively closer to each other in MC3E as compared to the ones in OLYMPEx (see Fig. 3), noticeable changes of rainfall statistics are observed across rain gauge sites (see Table 1). This may be explained by the variation of DSDs reported within the footprint of the dual-polarization weather radar (see Tokay et al. 2017). Among all of the rain gauges considered in MC3E, gauge 10 has the highest NB and NSE values for all of the algorithms. A single event that occurred in the late morning of 24 April 2011 (UTC) is considered to be the reason for this observation. Some of the radar measurements were missing and the rain rate changed rapidly during the event. Since the number of the remaining available radar scans was limited, the time history of such rapid changing rain rate (and hence, rainfall accumulations) could not be reconstructed accurately through linear interpolations of the radar estimations. To demonstrate the impacts of the differences in event characteristics on the performance of the algorithms, Table 3 was created. Similar statistical information as in Table 1 is provided for the five days of events at all 16 rain gauge

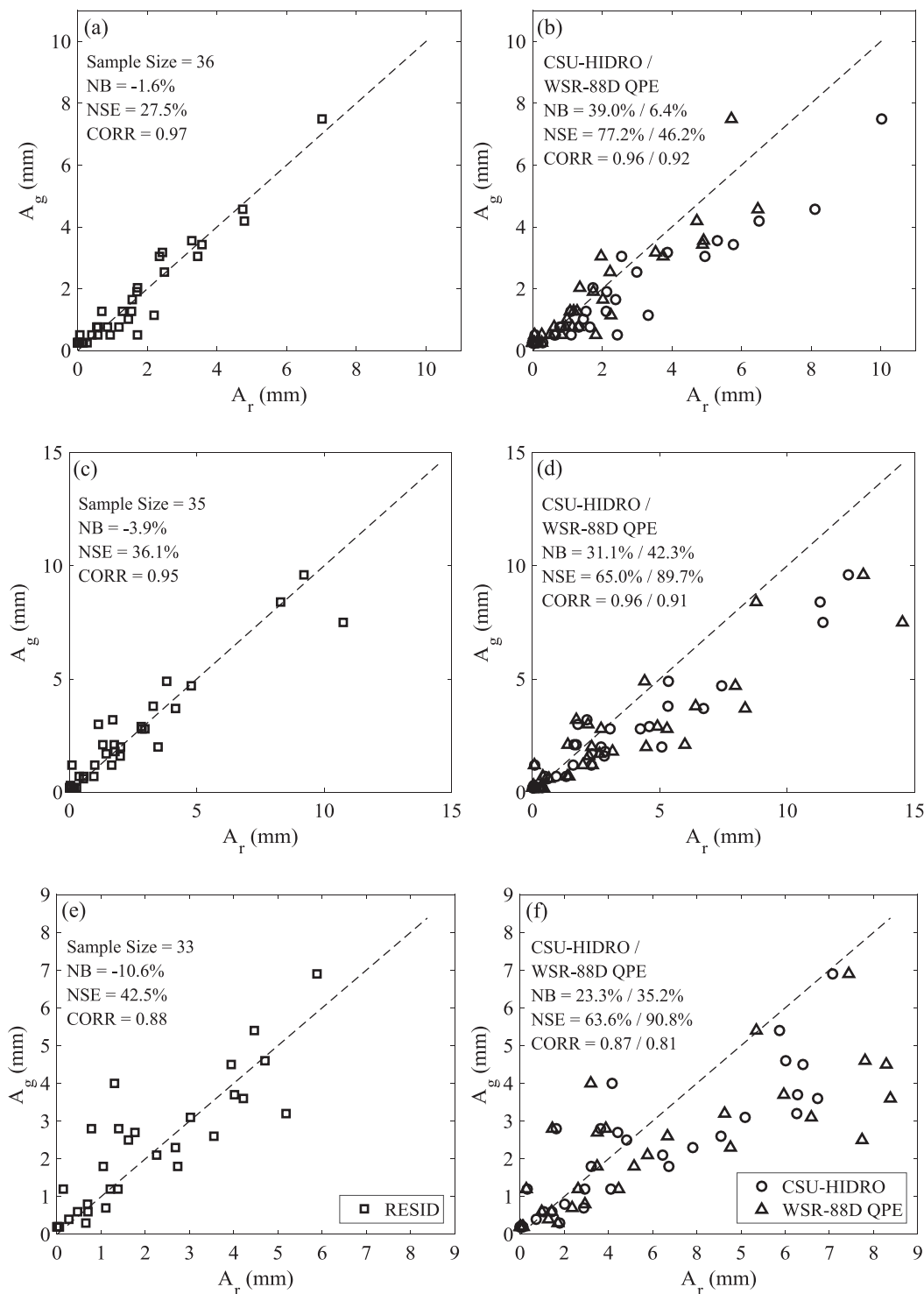


FIG. 5. Comparisons between A_g and A_r using RESID, CSU-HIDRO, and WSR-88D QPE algorithms at three sample locations in MC3E [(a),(b) for rain gauge pair 3; (c),(d) for rain gauge pair 11; (e),(f) for rain gauge pair 16]. Summarized statistics are given in Table 1.

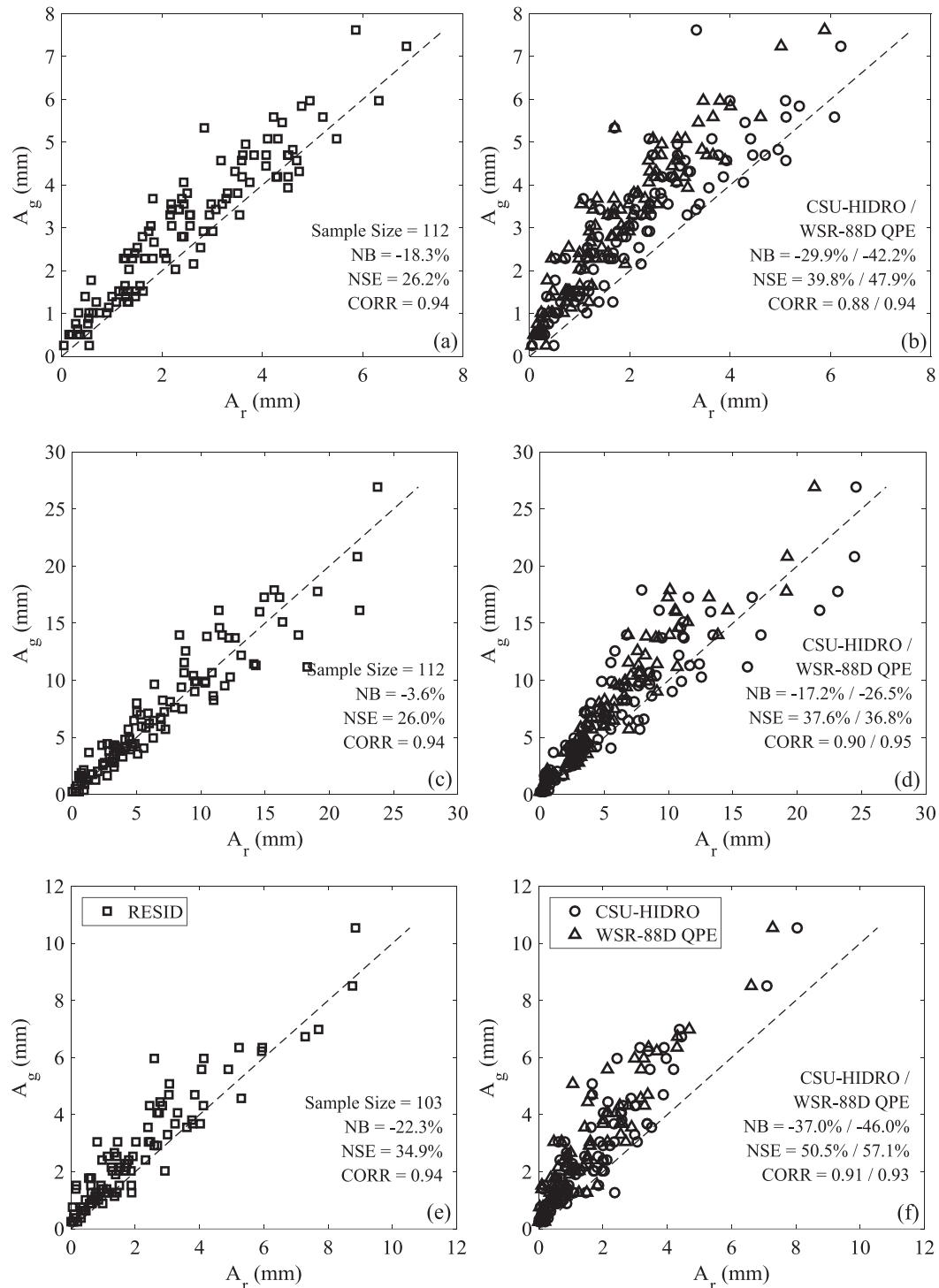


FIG. 6. As in Fig. 5, but for locations in OLYMPEx [(a),(b) for rain gauge pair 2; (c),(d) for rain gauge pair 4; (e),(f) for rain gauge pair 6]. Summarized statistics are given in Table 2.

locations of MC3E. The event characteristics shown in Table 3 were adopted from Jensen et al. (2016). As can be seen in this table, the statistics change significantly across the days of events. RESID, and the two

benchmark algorithms, performed better in terms of NSE values in both convective and stratiform events than the events with weak rainfall that occurred on 24 April. This behavior may be due to the presence

TABLE 1. Statistics between rain gauge-measured and radar-estimated rainfall accumulations in MC3E using RESID, CSU-HIDRO, and WSR-88D QPE algorithms.

Gauges/ statistics	NB (%)			NSE (%)			CORR			N^b	L_r^c	H_b^d
	RESID	CSU- HIDRO	WSR- 88D QPE	RESID	CSU- HIDRO	WSR- 88D QPE	RESID	CSU- HIDRO	WSR-88D QPE			
1	1.4	40.0	18.6	35.3	83.6	66.1	0.95	0.93	0.85	36	60	848
2	-3.7	34.8	32.5	41.1	82.3	77.4	0.93	0.92	0.92	34	57	789
3	-1.6	39.0	6.4	27.5	77.2	46.2	0.97	0.96	0.92	36	57	796
4	-5.4	32.9	5.7	31.5	71.8	54.3	0.95	0.94	0.87	31	60	845
5	-2.0	40.1	12.0	37.5	60.8	47.9	0.94	0.94	0.90	19	56	766
6	-4.7	41.1	9.8	29.1	74.8	51.2	0.96	0.96	0.89	30	54	725
7	-2.3	33.0	22.4	49.0	76.0	76.4	0.91	0.90	0.83	32	53	719
8	4.1	43.5	43.6	56.1	98.3	96.6	0.90	0.91	0.90	36	56	769
9 ^a	-16.0	27.8	37.7	29.3	38.9	51.8	0.87	0.93	0.94	8	59	814
10	12.3	49.0	52.0	81.0	125.1	137.9	0.87	0.89	0.85	37	58	792
11	-3.9	31.1	42.3	36.1	65.0	89.7	0.95	0.96	0.91	35	59	802
12	-9.3	22.0	34.9	39.3	53.5	78.1	0.93	0.94	0.92	31	61	831
13	-8.1	26.6	28.4	38.2	63.2	76.4	0.95	0.94	0.90	37	62	867
14	-4.1	24.7	8.9	56.2	65.1	68.5	0.81	0.87	0.76	30	65	906
15	1.5	35.1	32.8	42.8	73.5	78.0	0.89	0.90	0.87	30	65	909
16	-10.6	23.3	35.2	42.5	63.6	90.8	0.88	0.87	0.81	33	63	884
Mean	-2.5	34.4	25.8	42.8	75.4	75.6	0.92	0.92	0.87	32	59	817

^a Statistics discarded because of insufficient data samples.^b Sample size.^c Distance to radar (km).^d Beam height above ground (m).

of a large number of small drops in weak rainfall events. Similar behavior was observed in OLYMPEx and is discussed next in this section. Note that this observation may also explain the large NSE values (e.g., >50%) for RESID estimations at a few other locations given in Table 1.

- 2) For OLYMPEx (see Table 2), although the RESID algorithm outperforms the CSU-HIDRO and the WSR-88D QPE algorithms in all cases, its performance is not as high as that for MC3E (presented in Table 1). These conclusions are evident by compar-

ing the statistical results in Tables 1 and 2 as well as the visual representations in Figs. 5 and 6. Figure 7 presents the RESID statistics for the two field campaigns as a function of rain gauge distance to the radar and beam height above ground. This figure provides a means to compare the performance of RESID in two different field campaigns by taking into account the sources of discrepancies (i.e., rain gauge distance to the radar and beam height above ground). Each data point shown in Fig. 7 represents an individual rain gauge. The beam height above

TABLE 2. As in Table 1, but for locations in OLYMPEx.

Gauges/ Statistics	NB (%)			NSE (%)			CORR			N^a	L_r^b	H_b^c
	RESID	CSU- HIDRO	WSR- 88D QPE	RESID	CSU- HIDRO	WSR-88D QPE	RESID	CSU- HIDRO	WSR-88D QPE			
1	-32.6	-42.7	-52.6	44.6	53.0	61.9	0.87	0.88	0.93	113	51	561
2	-18.3	-29.9	-42.2	26.2	39.8	47.9	0.94	0.88	0.94	112	52	639
3	-20.4	-33.2	-35.8	32.9	45.4	44.9	0.91	0.88	0.93	108	28	342
4	-3.6	-17.2	-26.5	26.0	37.6	36.8	0.94	0.90	0.95	112	50	612
5	-24.8	-33.5	-48.0	34.0	43.5	56.2	0.92	0.88	0.91	114	50	612
6	-22.3	-37.0	-46.0	34.9	50.5	57.1	0.94	0.91	0.93	103	58	815
7	-18.5	-31.6	-40.8	29.2	41.0	49.8	0.95	0.93	0.95	109	42	519
8	-28.3	-33.7	-56.4	40.9	44.4	71.1	0.95	0.95	0.92	108	17	194
Mean	-21.1	-32.4	-43.5	33.6	44.4	53.2	0.93	0.90	0.93	110	43	537

^a Sample size.^b Distance to radar (km).^c Beam height above ground (m).

TABLE 3. As in Table 1, but for days of events (in 2011) instead of locations.

Event	Characteristics/ statistics	NB (%)			NSE (%)			CORR			Sample size
		RESID	CSU-HIDRO	WSR-88D QPE	RESID	CSU-HIDRO	WSR-88D QPE	RESID	CSU-HIDRO	WSR-88D QPE	
24 Apr	Elevated weak rain	12.0	45.8	53.6	88.0	126.1	151.5	0.89	0.91	0.90	59
25 Apr	Convective line/cell events	-12.1	16.6	-10.5	50.3	79.6	56.8	0.94	0.94	0.93	118
27 Apr	Widespread stratiform rain	-9.6	6.1	-11.6	51.4	49.7	44.9	0.73	0.78	0.78	110
11 May	Convective line/cell events	11.2	58.8	48.2	29.9	75.2	70.1	0.92	0.94	0.91	80
20 May	Convective line/cell events	-1.1	50.7	62.3	23.9	67.5	83.6	0.91	0.90	0.87	128
	Mean	0.1	35.6	28.4	48.7	79.6	81.4	0.88	0.89	0.88	99

ground was calculated using the following equation, suggested by the NWS (2017b) for the WSR-88D by assuming standard atmospheric conditions:

$$H_b = 1000 \left(L_r \sin \varphi + \frac{L_r^2}{2nR_e} \right) + H_a - E_b. \quad (17)$$

Here, H_b is the height from the radar beam centerline to the ground (m); L_r is the distance from the radar to the rain gauge site (km); φ is the radar elevation angle (taken as 0.5° in this study); n is the refractive index (assumed as 1.21); R_e is the radius of Earth (taken as 6371 km); and H_a and E_b are the radar antenna height and the ground elevation of the rain gauge site above mean sea level (m), respectively. The H_a values were found from the NWS (NWS 2016), and the E_b values were obtained using the one-third arc-second ground elevation data from the U.S. Geological Survey (USGS 2017). It can be seen from this figure that, for the rain gauges with similar L_r and H_b values, while the NSE values are similar for both field campaigns, the absolute values of NB are significantly lower for MC3E than for OLYMPEx (except for gauge 10 of MC3E as discussed above). Particularly, when L_r is larger than 45 km, the mean NB values for the RESID estimations are -2.5% for MC3E and -20.3% for OLYMPEx. This significant difference may be due to MC3E and OLYMPEx having different rainfall characteristics. The percentages of the radar observations that used different cost functions in RESID estimations and different rain-rate estimators in CSU-HIDRO estimations are presented in Table 4. As can be seen in this table, while the RESID estimations utilized the $CF(Z_h, Z_{dr})$ cost function for nearly 70% of the time in MC3E, the most frequently used cost function in OLYMPEx was $CF(Z_h)$ ($\sim 62\%$ of the time). This difference in the cost function usage is because of a larger number of small Z_h (< 38 dBZ) and Z_{dr} (< 0.5 dB) values in OLYMPEx than MC3E (see Fig. 2). The larger errors in RESID estimations in OLYMPEx than in MC3E may be associated with the smaller Z_h and Z_{dr} values in OLYMPEx, which typically represent rainfall events with a presence of abundant small drops (e.g., drizzle). This is consistent with the meteorological conditions observed in the two field campaigns.

- 3) CSU-HIDRO performed better than WSR-88D QPE for some of the cases (see the statistical results presented in Tables 1 and 2). The performance of the CSU-HIDRO was indeed expected to be better than that of the WSR-88D QPE. It is because CSU-HIDRO is an algorithm that utilizes a combination of rain-rate estimators (see Fig. 1) to optimize the rainfall

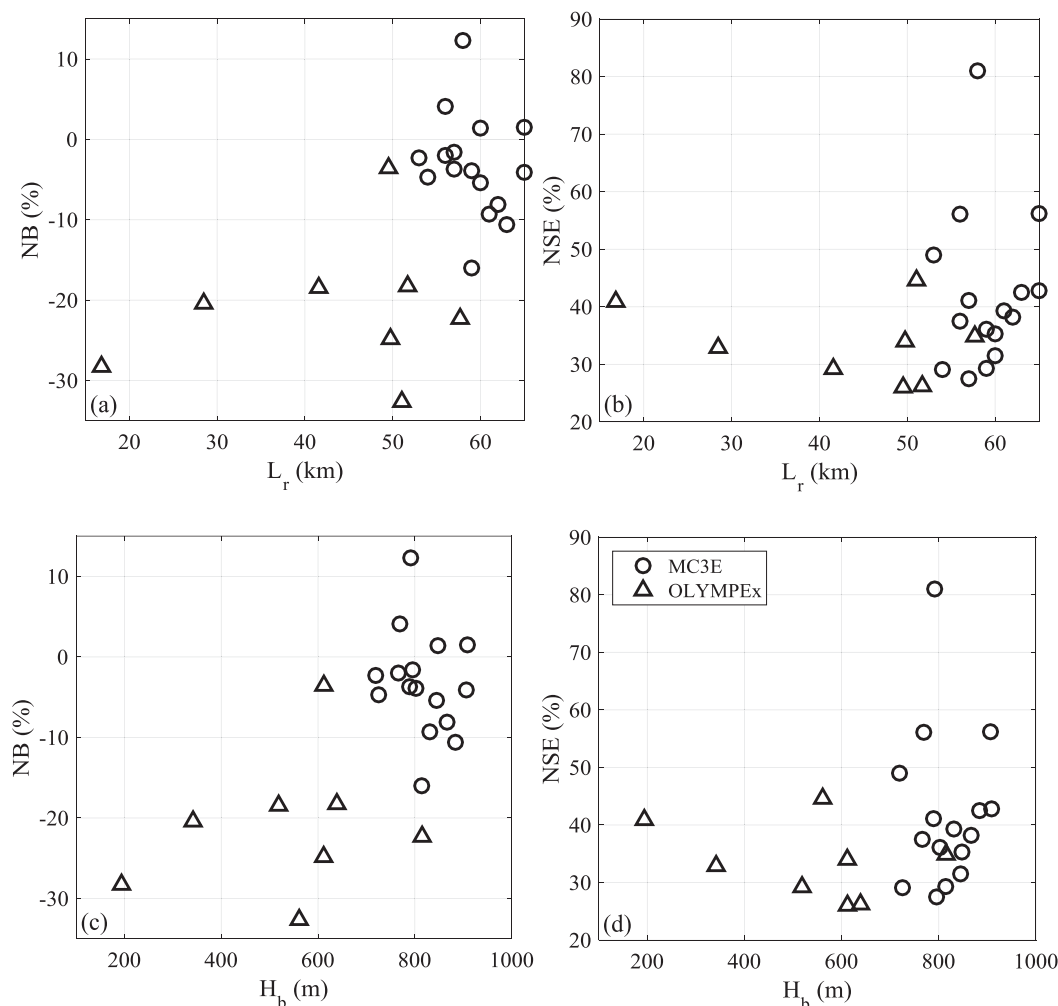


FIG. 7. (left) NB and (right) NSE for RESID estimations as a function of (a),(b) L_r and (c),(d) H_b for MC3E and OLYMPEx field campaigns. Open circles represent MC3E data and open triangles represent OLYMPEx data (see the legend). Each marker represents data for an individual rain gauge.

estimations (Cifelli et al. 2011), whereas WSR-88D QPE uses only the $R(Z_h, Z_{dr})$ estimator [see Eq. (3)] for liquid precipitation. The WSR-88D QPE estimations may suffer from the measurement errors when Z_{dr} values are relatively small. Moreover, it has been reported that when the K_{dp} values are relatively large, the rain-rate estimators using K_{dp} have the lowest amount of errors as compared to the other estimators (Brangi and Chandrasekar 2001; Cifelli et al. 2011). A lack of using such estimators in WSR-88D QPE may lead to less accurate rainfall estimations. Nevertheless, all of these rain-rate estimators were derived based upon the gamma DSD assumption. Our preliminary comparisons of the measured DSDs with the gamma DSD indicated that this assumption may underperform for some of the rainfall events in both MC3E and OLYMPEx, which

may have caused CSU-HIDRO to perform worse than WSR-88D QPE ($\sim 25\%$ of the cases for MC3E and OLYMPEx combined; see Tables 1 and 2). The deviation of the measured DSDs from the gamma distribution assumption has been reported in a number of studies (e.g., Zrníc et al. 2000; Mallet and Barthes 2009; D'Adderio et al. 2015; Adirosi et al. 2015, 2016). Among these studies Adirosi et al. (2015, 2016) investigated the accuracy of four different probability distribution functions (i.e., Pareto, log-normal, gamma, and Weibull distributions) in modeling the measured DSDs at three of the GPM field campaigns. Their results indicated that, in general, the distribution functions with a lighter tail (i.e., thinner than the tail of an exponential distribution, e.g., gamma distribution) showed a better agreement with the measurements. Nevertheless, there were also

TABLE 4. Percentages of radar observations that used different cost functions in RESID retrievals and different rain-rate estimators in CSU-HIDRO retrievals in MC3E and OLYMPEX. WSR-88D QPE used only the $R(Z_h, Z_{dr})$ estimator for liquid rainfall.

Field campaigns	Algorithms/%	$R(Z_h)/CF(Z_h)$	$R(Z_h, Z_{dr})/CF(Z_h, Z_{dr})$	$R(K_{dp})/CF(K_{dp})$	$R(K_{dp}, Z_{dr})/CF(K_{dp}, Z_{dr})$	$CF(Z_h, Z_{dr}, K_{dp})$
MC3E	RESID	26.02	69.22	0	1.39	3.37
	CSU-HIDRO	26.02	69.22	0	4.76	—
OLYMPEX	RESID	61.69	37.44	0.04	0.09	0.74
	CSU-HIDRO	61.69	37.44	0.04	0.83	—

DSD measurements from these field campaigns that showed significant deviations from the light-tailed distributions. The deviations from the assumed DSD form may also explain the increased errors of the RESID algorithm in OLYMPEX, as the simulated DSDs used in RESID are all gamma DSDs. When comparing the performance of the CSU-HIDRO and the WSR-88D QPE algorithms, one may notice that some of the NB values for CSU-HIDRO are higher than the numbers reported in Cifelli et al. (2011), and the NSE values for WSR-88D QPE are close to or larger than 100% for a few cases (see Tables 1 and 2). The reason for these is that comparisons in this study were rather stringent—hourly rainfall accumulations at each of the individual rain gauge locations were compared. Note that algorithms overestimate (with positive NBs) and underestimate (with negative NBs) rain rates at different times and different locations with varying standard errors. Comparing rainfall accumulations with longer durations (e.g., per event) and at multiple locations combined tends to balance the standard error and reduce the NB value in an absolute manner. Taking this fact into account, the NSE values for WSR-88D QPE are comparable to those reported in Giangrande et al. (2014).

- 4) It can be seen from Table 1 that RESID has both positive and negative NB values, which indicates that it overestimated rainfall accumulations for some cases and underestimated them for the others. However, all of the NB values for the CSU-HIDRO and the WSR-88D QPE estimations are positive in MC3E and negative in OLYMPEX (see Tables 1 and 2). This finding indicates that estimations from these two algorithms always overestimated the rainfall accumulations in MC3E but underestimated them in OLYMPEX. As presented in Table 4, the most frequently used rain-rate estimators by CSU-HIDRO in MC3E and OLYMPEX are $R(Z_h, Z_{dr})$ and $R(Z_h)$, respectively. Here it is important to reiterate that $R(Z_h, Z_{dr})$ is the only estimator used by the WSR-88D QPE to estimate liquid rainfall. Giangrande et al. (2014) discussed that KVN products over- and underestimated radar rainfall in MC3E at relatively low and high rain gauge accumulations, respectively. This finding is in agreement with what was observed here, that the overestimations by CSU-HIDRO and WSR-88D QPE in MC3E were caused by the usage of $R(Z_h, Z_{dr})$, which overestimated at relatively low rainfall accumulations (see Figs. 5, 6). The underestimation of $R(Z_h)$ for events with a large number of small drops (i.e., low Z_{dr} values; see the discussion above) was also reported (e.g., Ryzhkov et al. 2005a), and it is also consistent with the findings of

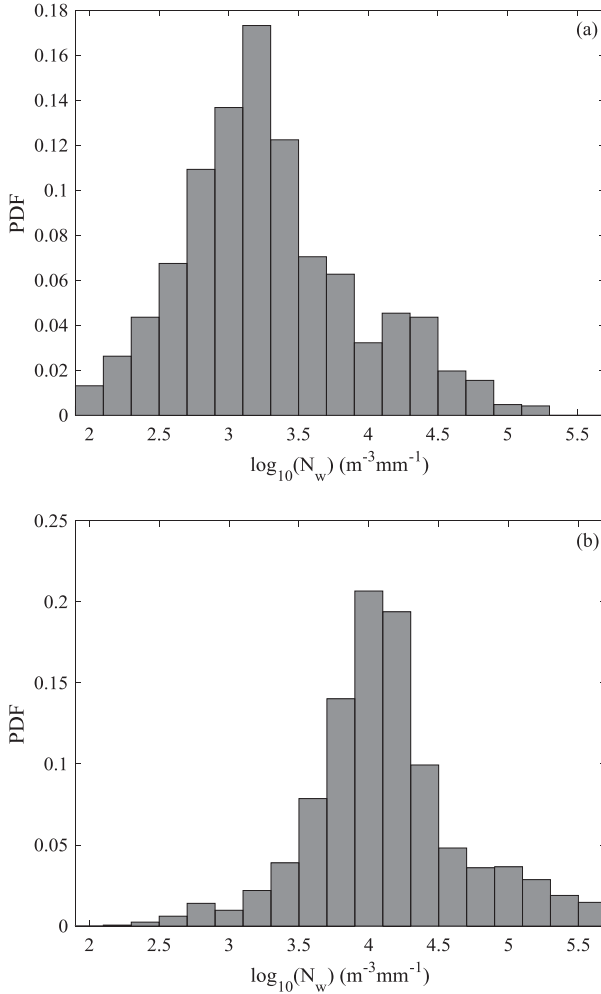


FIG. 8. PDFs of estimated $\log_{10}(N_w)$ values using 2DVD measurements from (a) MC3E and (b) OLYMPEx field experiments.

our study for OLYMPEx. The causes of these over- and underestimations may be explained by Fig. 8. This figure presents two probability density functions (PDFs) of the $\log_{10}(N_w)$ values calculated using the DSD measurements from a two-dimensional video disdrometer (2DVD; Kruger and Krajewski 2002) in both MC3E and OLYMPEx. The distance from the disdrometer to rain gauge pair 1 in MC3E was about 1 km, and the disdrometer was collocated with rain gauge pair 3 in OLYMPEx (see Fig. 3). The DSD data that were used to plot Fig. 8 correspond to the same measurement periods as the radar and the rain gauge data that were utilized in this study. The N_w values were computed using the following equation (Bringi and Chandrasekar 2001):

$$N_w = \frac{3.67^4}{\pi \rho_w} \left(\frac{10^3 W}{D_0^4} \right) (\text{mm}^{-1} \text{m}^{-3}), \quad (18)$$

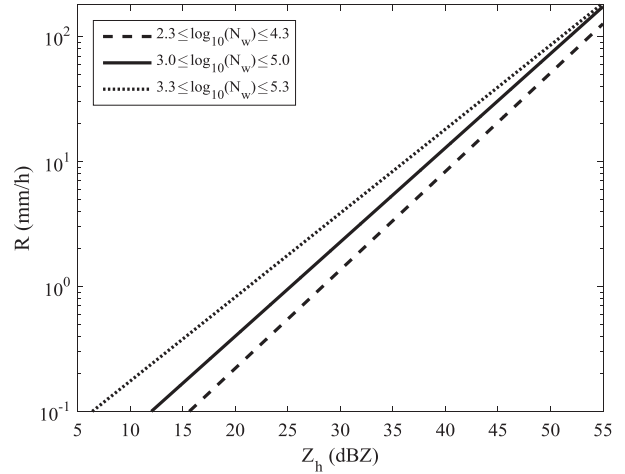


FIG. 9. Comparison of rain-rate estimations using the estimator $R(Z_h)$ derived using different ranges of $\log_{10}(N_w)$ (N_w values are in $\text{mm}^{-1} \text{m}^{-3}$).

where ρ_w is the water density (g cm^{-3}) and W is the liquid water content (g m^{-3}). The W and D_0 values were calculated using

$$W = \frac{\pi \rho_w}{6 \times 10^3} \int_0^\infty D^3 N(D) dD = \frac{\pi \rho_w}{3 \times 10^3} \int_0^{D_0} D^3 N(D) dD. \quad (19)$$

Similar to the DSD simulation procedure detailed in section 2, the range of the $\log_{10}(N_w)$ values selected for the derivation of the CSU-HIDRO/WSR-88D QPE rain-rate estimators was between 3 and 5 (for N_w in $\text{mm}^{-1} \text{m}^{-3}$; Bringi and Chandrasekar 2001). However, this range does not exactly match (i.e., skewed) the $\log_{10}(N_w)$ ranges calculated from 2DVD measurements at the field campaigns. Most (>90%) of the measured $\log_{10}(N_w)$ values were between 2.3 and 4.3 in MC3E and between 3.3 and 5.3 (for N_w in $\text{mm}^{-1} \text{m}^{-3}$) in OLYMPEx (see Fig. 8). A comparison of rain-rate estimations using $R(Z_h)$ derived using different ranges of $\log_{10}(N_w)$ (keeping the same value ranges for other parameters) is presented in Fig. 9. It can be seen from Fig. 9 that for a given Z_h , the estimated rain rate R increases with the following order of the $\log_{10}(N_w)$ range: 2.3–4.3 (from MC3E measurements), 3.0–5.0 (used for developing CSU-HIDRO/WSR-88D QPE estimators), and 3.3–5.3 (from OLYMPEx measurements) (for N_w in $\text{mm}^{-1} \text{m}^{-3}$). Similar behaviors were observed for other rain-rate estimators. This is likely the reason why CSU-HIDRO and WSR-88D QPE overestimated the rainfall accumulations for MC3E but underestimated them for OLYMPEx. Therefore, the over- and underestimation issue discussed above was likely caused by the regression analyses using the selected ranges of the gamma distribution parameters.

Since regression analysis was not incorporated in the development of RESID, this issue is inherently absent in RESID. This may also partly explain why RESID outperformed CSU-HIDRO and WSR-88D QPE in estimating the rainfall accumulations at both of the field campaigns.

5. Summary and conclusions

We developed a new rainfall estimation algorithm, RESID, for dual-polarization radars. We showed that the RESID algorithm, which utilizes a database of simulated gamma DSDs and a group of carefully selected cost functions, outperforms the benchmark CSU-HIDRO and WSR-88D QPE algorithms in estimating the hourly rainfall accumulations for the rain events observed during the MC3E and the OLYMPEx field campaigns. The likely reasons for the improved estimations by RESID are the fact that this hybrid algorithm is not subject to the regression uncertainties associated with other algorithms and reduces the potential impacts of noisy radar measurements.

Nevertheless, like all other algorithms, RESID has shortcomings. There are two major error sources for RESID estimations: one is related to the gamma distribution assumption in the DSD simulations and the other one is related to the cost functions that use fewer than three radar observables. Although the gamma distribution is nowadays a widely used distribution to describe the DSD shape, the exponential (Marshall and Palmer 1948), lognormal (Feingold and Levin 1986), and Gaussian (Maguire and Avery 1994) distributions are also possible distribution functions to model the observed DSDs. In this study, the values of the cost functions were not a major focus. Although larger errors in rainfall estimations were expected for larger values of the cost functions, the majority (~95%) of the cost function values observed in this study were less than 0.001, which indicates a close match between the measured and the simulated DSDs (see Adirosi et al. 2014). If the cost function values can be reduced by using a simulated DSD database of a different distribution function, the radar rainfall estimations may be further improved. Moreover, we used different cost functions under different conditions to reduce the impact of the radar measurement noise. The reason we used the single- and double-measurement cost functions was because we found out that the errors introduced by these cost functions were smaller than the errors introduced by the triple-measurement cost function when a particular radar observable(s) was not reliable. If the RESID were developed for DSD retrievals, the use of the triple-measurement cost function would have been advantageous over the single- and double-measurement cost functions, as the triple-measurement cost function

provides more information. However, since RESID was developed for radar rainfall estimations, it uses a set of cost functions with a varying number of radar observables to reduce the effect of noisy radar measurements. As such, while the selected simulated DSDs may not necessarily match closely with the measured DSDs because fewer radar observables may have been used, the rain rates calculated from these selected DSDs are expected to closely estimate the actual rain-rate values.

The RESID algorithm was thoroughly evaluated using the observations from the MC3E and the OLYMPEx field campaigns, and these evaluations showed favorable results as discussed in detail in section 4. There is still potential for further improvements of the algorithm. These improvements may include development of new cost functions for reduced radar observational uncertainties and a more robust scheme for homogeneity confinement of DSDs. Further performance evaluations of RESID under different environmental and meteorological conditions and at different geographic locations are also necessary. The improved radar rainfall estimations using RESID are of great practical significance in a wide variety of fields, including flash-flood warning and management, water resources management, and climate change evaluation.

Acknowledgments. This research was supported by the funds provided by the National Science Foundation under Grants AGS-1612681, AGS-1144846, and AGS-1741250 to the second author (FYT). The first author was a graduate student under the guidance of FYT.

REFERENCES

- Adirosi, E., E. Gorgucci, L. Baldini, and A. Tokay, 2014: Evaluation of gamma raindrop size distribution assumption through comparison of rain rates of measured and radar-equivalent gamma DSD. *J. Appl. Meteor. Climatol.*, **53**, 1618–1635, <https://doi.org/10.1175/JAMC-D-13-0150.1>.
- , L. Baldini, F. Lombardo, F. Russo, F. Napolitano, E. Volpi, and A. Tokay, 2015: Comparison of different fittings of drop spectra for rainfall retrievals. *Adv. Water Resour.*, **83**, 55–67, <https://doi.org/10.1016/j.advwatres.2015.05.009>.
- , E. Volpi, F. Lombardo, and L. Baldini, 2016: Raindrop size distribution: Fitting performance of common theoretical models. *Adv. Water Resour.*, **96**, 290–305, <https://doi.org/10.1016/j.advwatres.2016.07.010>.
- Atlas, D., and C. W. Ulbrich, 1977: Path- and area-integrated rainfall measurement by microwave attenuation in the 1–3 cm band. *J. Appl. Meteor.*, **16**, 1322–1331, [https://doi.org/10.1175/1520-0450\(1977\)016<1322:PAAIRM>2.0.CO;2](https://doi.org/10.1175/1520-0450(1977)016<1322:PAAIRM>2.0.CO;2).
- , R. C. Srivastava, and R. S. Sckhon, 1973: Doppler radar characteristics of precipitation at vertical incidence. *Rev. Geophys. Space Phys.*, **11**, 1–35, <https://doi.org/10.1029/RG011i001p00001>.
- Aydin, K., V. N. Bringi, and L. Liu, 1995: Estimation of rain and hail rates in mixed-phase precipitation. *J. Appl. Meteor.*, **34**, 404–410, <https://doi.org/10.1175/1520-0450-34.2.404>.

- Beard, K. V., and A. R. Jameson, 1983: Raindrop canting. *J. Atmos. Sci.*, **40**, 448–454, [https://doi.org/10.1175/1520-0469\(1983\)040<0448:RC>2.0.CO;2](https://doi.org/10.1175/1520-0469(1983)040<0448:RC>2.0.CO;2).
- , and C. Chuang, 1987: A new model for the equilibrium shape of raindrops. *J. Atmos. Sci.*, **44**, 1509–1524, [https://doi.org/10.1175/1520-0469\(1987\)044<1509:ANMFTE>2.0.CO;2](https://doi.org/10.1175/1520-0469(1987)044<1509:ANMFTE>2.0.CO;2).
- , V. N. Bringi, and M. Thurai, 2010: A new understanding of raindrop shape. *Atmos. Res.*, **97**, 396–415, <https://doi.org/10.1016/j.atmosres.2010.02.001>.
- Berkowitz, D. S., J. A. Schultz, S. Vasiloff, K. L. Elmore, C. D. Payne, and J. B. Boettcher, 2013: Status of dual pol QPE in the WSR-88D network. *27th Conf. on Hydrology*, Austin, TX, Amer. Meteor. Soc., 2.2, <https://ams.confex.com/ams/93Annual/webprogram/Paper221525.html>.
- Brandes, E. A., G. Zhang, and J. Vivekanandan, 2004a: Drop size distribution retrieval with polarimetric radar: Model and application. *J. Appl. Meteor.*, **43**, 461–475, [https://doi.org/10.1175/1520-0450\(2004\)043<0461:DSDRWP>2.0.CO;2](https://doi.org/10.1175/1520-0450(2004)043<0461:DSDRWP>2.0.CO;2).
- , —, and —, 2004b: Comparison of polarimetric radar drop size distribution retrieval algorithms. *J. Atmos. Oceanic Technol.*, **21**, 584–598, [https://doi.org/10.1175/1520-0426\(2004\)021<0584:COPRDS>2.0.CO;2](https://doi.org/10.1175/1520-0426(2004)021<0584:COPRDS>2.0.CO;2).
- Bringi, V. N., and V. Chandrasekar, 2001: *Polarimetric Doppler Weather Radar: Principles and Applications*. Cambridge University Press, 636 pp.
- , L. Liu, P. C. Kennedy, V. Chandrasekar, and S. A. Rutledge, 1996: Dual multiparameter radar observations of intense convective storms: The 24 June 1992 case study. *Meteor. Atmos. Phys.*, **59**, 3–31, <https://doi.org/10.1007/BF01031999>.
- , G. Huang, V. Chandrasekar, and E. Gorgucci, 2002: A methodology for estimating the parameters of a gamma raindrop size distribution model from polarimetric radar data: Application to a squall-line event from the TRMM/Brazil campaign. *J. Atmos. Oceanic Technol.*, **19**, 633–645, [https://doi.org/10.1175/1520-0426\(2002\)019<0633:AMFETP>2.0.CO;2](https://doi.org/10.1175/1520-0426(2002)019<0633:AMFETP>2.0.CO;2).
- , V. Chandrasekar, J. Hubbard, E. Gorgucci, W. Randeu, and M. Schoenhuber, 2003: Raindrop size distribution in different climate regimes from disdrometer and dual-polarized radar analysis. *J. Atmos. Sci.*, **60**, 354–365, [https://doi.org/10.1175/1520-0469\(2003\)060<0354:RSDIDC>2.0.CO;2](https://doi.org/10.1175/1520-0469(2003)060<0354:RSDIDC>2.0.CO;2).
- , C. R. Williams, M. Thurai, and P. T. May, 2009: Using dual-polarized radar and dual-frequency profiler for DSD characterization: A case study from Darwin, Australia. *J. Atmos. Oceanic Technol.*, **26**, 2107–2122, <https://doi.org/10.1175/2009JTECHA1258.1>.
- Cao, Q., G. Zhang, E. A. Brandes, and T. J. Schuur, 2010: Polarimetric radar rain estimation through retrieval of drop size distribution using a Bayesian approach. *J. Appl. Meteor. Climatol.*, **49**, 973–990, <https://doi.org/10.1175/2009JAMC2227.1>.
- Chandrasekar, V., E. Gorgucci, and G. Scarchilli, 1993: Optimization of multiparameter radar estimates of rainfall. *J. Appl. Meteor.*, **32**, 1288–1293, [https://doi.org/10.1175/1520-0450\(1993\)032<1288:OOMREO>2.0.CO;2](https://doi.org/10.1175/1520-0450(1993)032<1288:OOMREO>2.0.CO;2).
- Ciach, G. J., M. L. Morrissey, and W. F. Krajewski, 2000: Conditional bias in radar rainfall estimation. *J. Appl. Meteor.*, **39**, 1941–1946, [https://doi.org/10.1175/1520-0450\(2000\)039<1941:CBIRRE>2.0.CO;2](https://doi.org/10.1175/1520-0450(2000)039<1941:CBIRRE>2.0.CO;2).
- Cifelli, R., W. A. Petersen, L. D. Carey, and S. A. Rutledge, 2002: Radar observations of the kinematic, microphysical, and precipitation characteristics of two MCSs in TRMM LBA. *J. Geophys. Res.*, **107**, 8077, <https://doi.org/10.1029/2000JD000264>.
- , V. Chandrasekar, S. Lim, P. C. Kennedy, Y. Wang, and S. A. Rutledge, 2011: A new dual-polarization radar rainfall algorithm: Application in Colorado precipitation events. *J. Atmos. Oceanic Technol.*, **28**, 352–364, <https://doi.org/10.1175/2010JTECHA1488.1>.
- D’Adderio, L. P., F. Porcu, and A. Tokay, 2015: Identification and analysis of collisional breakup in natural rain. *J. Atmos. Sci.*, **72**, 3404–3416, <https://doi.org/10.1175/JAS-D-14-0304.1>.
- Dolan, B., S. A. Rutledge, S. Lim, V. Chandrasekar, and M. Thurai, 2013: A robust C-band hydrometeor identification algorithm and application to a long-term polarimetric radar dataset. *J. Appl. Meteor. Climatol.*, **52**, 2162–2186, <https://doi.org/10.1175/JAMC-D-12-0275.1>.
- Draine, B. T., and P. J. Flatau, 1994: Discrete-dipole approximation for scattering calculations. *J. Opt. Soc. Amer.*, **11A**, 1491–1499, <https://doi.org/10.1364/JOSAA.11.001491>.
- Feingold, G., and Z. Levin, 1986: The lognormal fit to raindrop spectra from frontal convective clouds in Israel. *J. Climate Appl. Meteor.*, **25**, 1346–1363, [https://doi.org/10.1175/1520-0450\(1986\)025<1346:TLFTRS>2.0.CO;2](https://doi.org/10.1175/1520-0450(1986)025<1346:TLFTRS>2.0.CO;2).
- Fulton, R. A., J. P. Breidenbach, D. J. Seo, D. A. Miller, and T. O’Bannon, 1998: The WSR-88D rainfall algorithm. *Wea. Forecasting*, **13**, 377–395, [https://doi.org/10.1175/1520-0434\(1998\)013<0377:TWRA>2.0.CO;2](https://doi.org/10.1175/1520-0434(1998)013<0377:TWRA>2.0.CO;2).
- Giangrande, S. E., and A. V. Ryzhkov, 2008: Estimation of rainfall based on the results of polarimetric echo classification. *J. Appl. Meteor. Climatol.*, **47**, 2445–2462, <https://doi.org/10.1175/2008JAMC1753.1>.
- , S. Collis, A. K. Theisen, and A. Tokay, 2014: Precipitation estimation from the ARM distributed radar network during the MC3E campaign. *J. Appl. Meteor. Climatol.*, **53**, 2130–2147, <https://doi.org/10.1175/JAMC-D-13-0321.1>.
- Global Hydrology Resource Center, 2017: GHRC documents. Accessed 20 October 2017, <https://ghrc.nsstc.nasa.gov/home/ghrcdocs>.
- Gorgucci, E., G. Scarchilli, V. Chandrasekar, and V. N. Bringi, 2000: Measurement of mean raindrop shape from polarimetric radar observations. *J. Atmos. Sci.*, **57**, 3406–3413, [https://doi.org/10.1175/1520-0469\(2000\)057<3406:MOMRSF>2.0.CO;2](https://doi.org/10.1175/1520-0469(2000)057<3406:MOMRSF>2.0.CO;2).
- , —, —, and —, 2001: Rainfall estimation from polarimetric radar measurements: Composite algorithms immune to variability in raindrop shape–size relation. *J. Atmos. Oceanic Technol.*, **18**, 1773–1786, [https://doi.org/10.1175/1520-0426\(2001\)018<1773:REFPRM>2.0.CO;2](https://doi.org/10.1175/1520-0426(2001)018<1773:REFPRM>2.0.CO;2).
- , V. Chandrasekar, V. N. Bringi, and G. Scarchilli, 2002: Estimation of raindrop size distribution parameters from polarimetric radar measurements. *J. Atmos. Sci.*, **59**, 2373–2384, [https://doi.org/10.1175/1520-0469\(2002\)059<2373:EORSDF>2.0.CO;2](https://doi.org/10.1175/1520-0469(2002)059<2373:EORSDF>2.0.CO;2).
- , —, and L. Baldini, 2008: Microphysical retrievals from dual-polarization radar measurements at X band. *J. Atmos. Oceanic Technol.*, **25**, 729–741, <https://doi.org/10.1175/2007JTECHA971.1>.
- Houze, R. A., Jr., and Coauthors, 2017: The Olympic Mountains Experiment (OLYMPEX). *Bull. Amer. Meteor. Soc.*, **98**, 2167–2188, <https://doi.org/10.1175/BAMS-D-16-0182.1>.
- Jensen, M. P., and Coauthors, 2016: The Midlatitude Continental Convective Clouds Experiment (MC3E). *Bull. Amer. Meteor. Soc.*, **97**, 1667–1686, <https://doi.org/10.1175/BAMS-D-14-00228.1>.
- Krajewski, W. F., and J. A. Smith, 2002: Radar hydrology: Rainfall estimation. *Adv. Water Resour.*, **25**, 1387–1394, [https://doi.org/10.1016/S0309-1708\(02\)00062-3](https://doi.org/10.1016/S0309-1708(02)00062-3).
- Kruger, A., and W. F. Krajewski, 2002: Two-dimensional video disdrometer: A description. *J. Atmos. Oceanic Technol.*, **19**,

- 602–617, [https://doi.org/10.1175/1520-0426\(2002\)019<0602:TDVDAD>2.0.CO;2](https://doi.org/10.1175/1520-0426(2002)019<0602:TDVDAD>2.0.CO;2).
- Leinonen, J., 2014: High-level interface to *T*-matrix scattering calculations: Architecture, capabilities and limitations. *Opt. Express*, **22**, 1655–1660, <https://doi.org/10.1364/OE.22.001655>.
- Lim, S., V. Chandrasekar, and V. N. Bringi, 2005: Hydrometeor classification system using dual-polarization radar measurements: Model improvements and in situ verification. *IEEE Trans. Geosci. Remote Sens.*, **43**, 792–801, <https://doi.org/10.1109/TGRS.2004.843077>.
- Maguire, W. B., and S. K. Avery, 1994: Retrieval of raindrop size distributions using two Doppler wind profilers: Model sensitivity testing. *J. Appl. Meteor.*, **33**, 1623–1635, [https://doi.org/10.1175/1520-0450\(1994\)033<1623:RORSDU>2.0.CO;2](https://doi.org/10.1175/1520-0450(1994)033<1623:RORSDU>2.0.CO;2).
- Mallet, C., and L. Barthes, 2009: Estimation of gamma raindrop size distribution parameters: Statistical fluctuations and estimation errors. *J. Atmos. Oceanic Technol.*, **26**, 1572–1584, <https://doi.org/10.1175/2009JTECHA1199.1>.
- Marshall, J. S., W. M. Palmer, 1948: The distribution of raindrops with size. *J. Meteor.*, **5**, 165–166, [https://doi.org/10.1175/1520-0469\(1948\)005<0165:TDORWS>2.0.CO;2](https://doi.org/10.1175/1520-0469(1948)005<0165:TDORWS>2.0.CO;2).
- Mass, C., 2011: Langley Hill coastal radar: The latest addition to the National Weather Service Doppler radar network. Accessed 22 January 2018, <https://www.atmos.washington.edu/cliff/Langleyradar.html>.
- McFarquhar, G. M., T. Hsieh, M. Freer, J. Mascio, and B. F. Jewett, 2015: The characterization of ice hydrometeor gamma size distributions as volumes in $N_{\sigma}-\lambda-\mu$ phase space: Implications for microphysical process modeling. *J. Atmos. Sci.*, **72**, 892–909, <https://doi.org/10.1175/JAS-D-14-0011.1>.
- Met One Instruments, Inc., 2017: 370–380 precipitation gauges. Accessed 20 October 2017, <http://metone.com/meteorological-sensors-systems/rain/370-380/>.
- Mishchenko, M. I., L. D. Travis, and D. W. Mackowski, 1996: *T*-matrix computations of light scattering by nonspherical particles: A review. *J. Quant. Spectrosc. Radiat. Transfer*, **55**, 535–575, [https://doi.org/10.1016/0022-4073\(96\)00002-7](https://doi.org/10.1016/0022-4073(96)00002-7).
- NWS, 2016: WSR-88D radar list (159 sites). Accessed 29 January 2018, 6 pp., <https://www.weather.gov/media/tg/wsr88d-radar-list.pdf>.
- , 2017a: Quick reference VCP comparison table for RPG operators. Accessed 12 May 2018, 1 pp., <https://training.weather.gov/wdtd/tools/RPS/VCPCompTable.pdf>.
- , 2017b: Beam property calculator: Origin of this application. Accessed 29 January 2018, <http://training.weather.gov/wdtd/tools/misc/beamwidth/index.htm>.
- Pei, B., F. Y. Testik, and M. Gebremichael, 2014: Impacts of raindrop fall velocity and axis ratio errors on dual-polarization radar rainfall estimation. *J. Hydrometeorol.*, **15**, 1849–1861, <https://doi.org/10.1175/JHM-D-13-0201.1>.
- Petersen, W. A., and M. Jensen, 2012: The NASA-GPM and DOE-ARM Midlatitude Continental Convective Clouds Experiment (MC3E). *The Earth Observer*, Vol. 24, No. 1, Science Communications Support Office, NASA Goddard Space Flight Center, Greenbelt, MD, 12–18.
- , and Coauthors, 1999: Mesoscale and radar observations of the Fort Collins flash flood of 28 July 1997. *Bull. Amer. Meteor. Soc.*, **80**, 191–216, [https://doi.org/10.1175/1520-0477\(1999\)080<0191:MAROOT>2.0.CO;2](https://doi.org/10.1175/1520-0477(1999)080<0191:MAROOT>2.0.CO;2).
- Posselt, D. J., X. Li, S. A. Tushaus, and J. R. Mecikalski, 2015: Assimilation of dual-polarization radar observations in mixed- and ice-phase regions of convective storms: Information content and forward model errors. *Mon. Wea. Rev.*, **143**, 2611–2636, <https://doi.org/10.1175/MWR-D-14-00347.1>.
- Ray, P. S., 1972: Broadband complex refractive indices of ice and water. *Appl. Opt.*, **11**, 1836–1844, <https://doi.org/10.1364/AO.11.001836>.
- Ryzhkov, A., and D. Zrnić, 1995: Precipitation and attenuation measurements at a 10-cm wavelength. *J. Appl. Meteor.*, **34**, 2121–2134, [https://doi.org/10.1175/1520-0450\(1995\)034<2120:PAAMAA>2.0.CO;2](https://doi.org/10.1175/1520-0450(1995)034<2120:PAAMAA>2.0.CO;2).
- , and —, 1996: Assessment of rainfall measurement that uses specific differential phase. *J. Appl. Meteor.*, **35**, 2080–2090, [https://doi.org/10.1175/1520-0450\(1996\)035<2080:AORMTU>2.0.CO;2](https://doi.org/10.1175/1520-0450(1996)035<2080:AORMTU>2.0.CO;2).
- , S. E. Giangrande, and T. J. Schuur, 2005a: Rainfall estimation with a polarimetric prototype of WSR-88D. *J. Appl. Meteor.*, **44**, 502–515, <https://doi.org/10.1175/JAM2213.1>.
- Ryzhkov, A. V., T. J. Schuur, D. W. Burgess, P. L. Heinselman, S. E. Giangrande, and D. S. Zrnić, 2005b: The Joint Polarization Experiment: Polarimetric rainfall measurements and hydrometeor classification. *Bull. Amer. Meteor. Soc.*, **86**, 809–824, <https://doi.org/10.1175/BAMS-86-6-809>.
- , M. Pinsky, A. Pokrovsky, and A. Khain, 2011: Polarimetric radar observation operator for a cloud model with spectral microphysics. *J. Appl. Meteor. Climatol.*, **50**, 873–894, <https://doi.org/10.1175/2010JAMC2363.1>.
- Ryzhkov, A., M. Diederich, P. Zhang, and C. Simmer, 2014: Potential utilization of specific attenuation for rainfall estimation, mitigation of partial beam blockage, and radar networking. *J. Atmos. Oceanic Technol.*, **31**, 599–619, <https://doi.org/10.1175/JTECH-D-13-00038.1>.
- Sachidananda, M., and D. S. Zrnić, 1987: Rain rate estimates from differential polarization measurements. *J. Atmos. Oceanic Technol.*, **4**, 588–598, [https://doi.org/10.1175/1520-0426\(1987\)004<0588:RREFDP>2.0.CO;2](https://doi.org/10.1175/1520-0426(1987)004<0588:RREFDP>2.0.CO;2).
- Seliga, T. A., and V. N. Bringi, 1976: Potential use of radar differential reflectivity measurements at orthogonal polarizations for measuring precipitation. *J. Appl. Meteor.*, **15**, 69–76, [https://doi.org/10.1175/1520-0450\(1976\)015<0069:PUORDR>2.0.CO;2](https://doi.org/10.1175/1520-0450(1976)015<0069:PUORDR>2.0.CO;2).
- Sene, K., 2009: *Hydrometeorology: Forecasting and Applications*. Springer, 368 pp.
- Testik, F. Y., and M. Gebremichael, Eds., 2010: *Rainfall: State of the Science*. *Geophys. Monogr.*, Vol. 191, Amer. Geophys. Union, 287 pp., <https://doi.org/10.1029/GM191>.
- Thurai, M., G. J. Huang, V. N. Bringi, W. L. Randeu, and M. Schönhuber, 2007: Drop shapes, model comparisons, and calculations of polarimetric radar parameters in rain. *J. Atmos. Oceanic Technol.*, **24**, 1019–1032, <https://doi.org/10.1175/JTECH2051.1>.
- , V. N. Bringi, L. D. Carey, P. Gatlin, E. Schultz, and W. A. Petersen, 2012: Estimating the accuracy of polarimetric radar-based retrievals of drop-size distribution parameters and rain rate: An application of error variance separation using radar-derived spatial correlations. *J. Hydrometeorol.*, **13**, 1066–1079, <https://doi.org/10.1175/JHM-D-11-070.1>.
- Tokay, A., L. P. D’Adderio, F. Porcù, D. B. Wolff, and W. A. Petersen, 2017: A field study of footprint-scale variability of raindrop size distribution. *J. Hydrometeorol.*, **18**, 3165–3179, <https://doi.org/10.1175/JHM-D-17-0003.1>.

- Ulbrich, C. W., 1983: Natural variations in the analytical form of the raindrop size distribution. *J. Climate Appl. Meteor.*, **22**, 1764–1775, [https://doi.org/10.1175/1520-0450\(1983\)022<1764:NVITAF>2.0.CO;2](https://doi.org/10.1175/1520-0450(1983)022<1764:NVITAF>2.0.CO;2).
- USGS, 2017: TNM elevation. Accessed 29 January 2018, <https://viewer.nationalmap.gov/theme/elevation>.
- Vasiloff, S., 2012: Evaluation of dual-polarization QPE: Initial results for spring and summer 2012. Final Rep., Memo. of Understanding Task 1.1, NOAA Radar Operations Branch, 48 pp.
- WDTB, 2011: Dual-polarization radar principles and system operations. Version 1109, National Weather Service Warning Decision Training Branch, 94 pp.
- Willis, P. T., 1984: Functional fits to some observed drop size distributions and parameterization of rain. *J. Atmos. Sci.*, **41**, 1648–1661, [https://doi.org/10.1175/1520-0469\(1984\)041<1648:FFTSOD>2.0.CO;2](https://doi.org/10.1175/1520-0469(1984)041<1648:FFTSOD>2.0.CO;2).
- Zhang, G., J. Vivekanandan, and E. Brandes, 2001: A method for estimating rain rate and drop size distribution from polarimetric radar measurements. *IEEE Trans. Geosci. Remote Sens.*, **39**, 830–841, <https://doi.org/10.1109/36.917906>.
- Zrnić, D. S., T. D. Keenan, L. D. Carey, and P. May, 2000: Sensitivity analysis of polarimetric variables at a 5-cm wavelength in rain. *J. Appl. Meteor.*, **39**, 1514–1526, [https://doi.org/10.1175/1520-0450\(2000\)039<1514:SAOPVA>2.0.CO;2](https://doi.org/10.1175/1520-0450(2000)039<1514:SAOPVA>2.0.CO;2).